# Improving Charge Transport in Integrated MoO<sub>3</sub>/C Electrode Materials for Water-In-Salt Energy Storage Systems by Incorporating Oxygen Vacancies

Farbod Alimohammadi<sup>1\*</sup>, Darrell Omo-Lamai<sup>1\*</sup>, Ryan Andris<sup>1</sup>, Timofey Averianov<sup>1</sup>, Zhongling Wang<sup>2,3</sup>, Lei Wang<sup>2,3</sup>, Kim Kisslinger<sup>4</sup>, Esther S. Takeuchi<sup>2,5,6,7</sup>, Amy C. Marschilok<sup>2,5,6,7</sup>, Kenneth J. Takeuchi<sup>2,5,6,7</sup>, Ekaterina Pomerantseva<sup>1\*\*</sup>

- Department of Materials Science and Engineering, Drexel University, Philadelphia, PA 19104, USA
- 2. Institute of Energy, Environment, Sustainability and Equity, Stony Brook University, Stony Brook, NY 11794, USA
- 3. Interdisciplinary Science Department, Brookhaven National Laboratory, Upton NY 11973
- 4. Center for Functional Nanomaterials, Brookhaven National Laboratory, Upton NY 11973
- 5. Department of Chemistry, Stony Brook University, Stony Brook, NY 11794, USA
- 6. Energy and Photon Sciences Directorate, National Synchrotron Light Source II, Brookhaven National Laboratory, Upton NY 11973, USA
- 7. Department of Materials Science and Chemical Engineering, Stony Brook University, Stony Brook, NY 11794, USA
- \* Farbod Alimohammadi and Darrell Omo-Lamai contributed equally to this work and designated as co-first authors
- \*\* Corresponding Author: ep423@drexel.edu

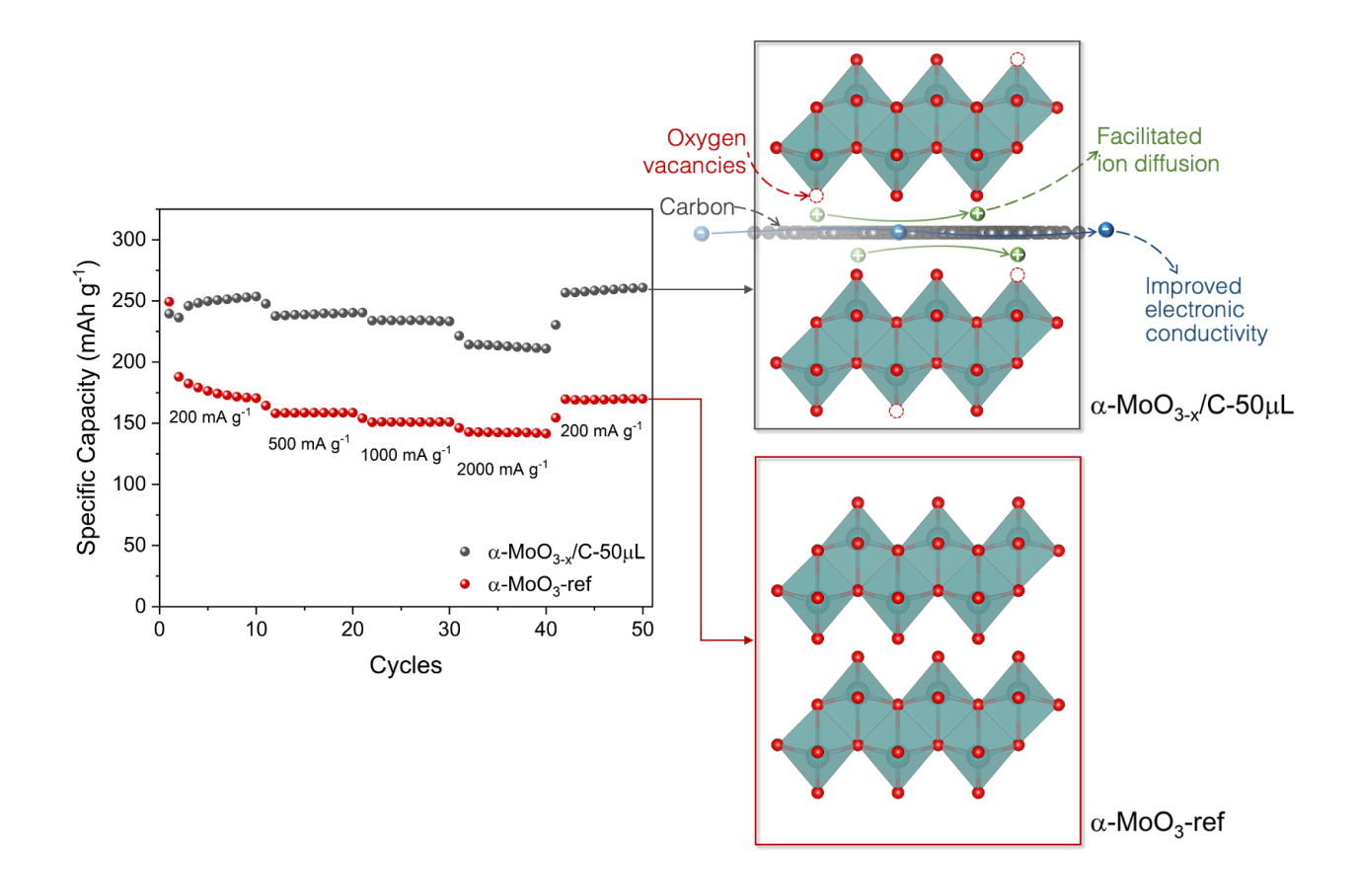
**Keywords:** MoO<sub>3</sub>; dopamine-derived carbon; oxygen vacancies; aqueous energy storage; water-in-salt electrolyte; charge transport properties

### **Abstract**

Improvements in the charge storage properties of α-MoO<sub>3</sub> used as an electrode with a 30m ZnCl<sub>2</sub> water-in-salt electrolyte have been achieved by enhancements in electron and ion transport enabled by an inventive synthesis route. Electron transport was improved through the integration of MoO<sub>3</sub> with dopamine-derived carbon via a chemical preintercalation route, and enhanced ion transport was achieved by incorporating oxygen vacancies in MoO<sub>3</sub> structure through ethanol

reduction under hydrothermal conditions. The presence of carbon was confirmed by corresponding D and G bands observed in Raman spectroscopy measurements. The presence of oxygen vacancies was proven through correlated XPS, TGA, Raman spectroscopy and XRD analyses, with the introduction of oxygen vacancies leading to an expanded interlayer region. Four-point probe measurements provided evidence of increased electronic conductivity due to the incorporation of carbon, and cyclic voltammetry-based charge storage mechanism analyses revealed increases in ion transport kinetics due to oxygen vacancy formation. Tuning the oxygen vacancy concentration is critical, as excessive concentrations of these point defects leads to structural instability and poor capacity retention. This work demonstrates the combined potential of carbon and oxygen vacancies in moderate concentrations to enhance the charge storage properties of transition metal oxides. The strategies developed in this study offer a path to the development of promising materials for high-rate, high-capacity, and long-duration electrochemical energy storage technologies.

# **Graphical Abstract**



#### Introduction

Advancements in energy storage technology are necessary to meet the growing demand for fast-charging portable electronic devices, reliable electric transportation, and grid infrastructure based on intermittent renewable energy sources<sup>1, 2</sup>. Li-ion batteries that utilize organic liquid electrolytes continue to be studied as energy storage devices due to their potential for high energy density and cycling stability, but the intrinsic flammability of the electrolytes contributes to safety concerns<sup>3-6</sup>. Aqueous rechargeable batteries (ARBs) attract attention due to the nonflammability of water-based electrolytes; the availability and facile processability of aqueous electrolyte components, leading to the reduction of their cost; their high tolerance to mechanical deformation, which makes them suitable for flexible and wearable electronics; and the high ionic conductivity of aqueous electrolytes, which enables high rate cycling and increased power density<sup>7-9</sup>.

Among the well-researched aqueous systems, Zn-based chemistries are particularly promising<sup>8</sup>. With a high volumetric capacity of 5855 mAh cm<sup>-3</sup>, a capability of reversible Zn stripping/plating in neutral and acidic environments, the divalent state of the Zn<sup>2+</sup> cation to which Zn oxidizes, and a standard reduction potential (-0.763 V versus the standard hydrogen electrode (SHE)) that is compatible with the electrochemical stability window of water, Zn metal is an attractive anode for high power ARBs<sup>10-13</sup>. However, further progress on in the development of complementary cathode materials is required to improve the viability of Zn-based ARBs.

 $\alpha$ -MoO<sub>3</sub> is a widely studied electrode material for electrochemical energy storage due to its high theoretical specific capacity relative to other transition metal oxides<sup>14, 15</sup>. It has an orthorhombic crystal structure that consists of a bilayer arrangement of edge-sharing MoO<sub>6</sub> octahedra held together along the b direction by van der Waals (vdW) interactions occurring between the layers<sup>16</sup> (**Figure S1, Supporting Information**). The interlayer region accommodates (de)intercalation of ions during electrochemical cycling. However, the charge storage properties of  $\alpha$ -MoO<sub>3</sub> are limited by its low intrinsic electronic conductivity, the irreversible deposition of electrochemically cycled ions in its structure during initial discharge cycles, and the cycling-induced collapse of its structure, leading to poor charge storage kinetics and rapid capacity fading<sup>17-19</sup>. Moreover, in low-to-moderate concentration aqueous electrolytes specifically, co-intercalation of water molecules due to the absence of a stable electrolyte interphase can lead to the dissolution of Mo, resulting in even more drastic cycling instability<sup>20,21</sup>.

One promising strategy to improve the charge storage properties of layered transition metal oxides (TMOs) with poor electronic conductivity involves chemically preintercalating organic molecule-derived carbon to form integrated TMO/C heterostructures in which electronic conductivity is improved due to the presence of the carbon component providing pathways for electron transport<sup>22-27</sup>. This approach was applied to the bilayered vanadium oxide ( $\delta$ -V<sub>2</sub>O<sub>5</sub>·nH<sub>2</sub>O) system. In a previous study, a 2D δ-C<sub>x</sub>V<sub>2</sub>O<sub>5</sub>·nH<sub>2</sub>O heterostructure was synthesized through the hydrothermal treatment of an aged solution that formed after the dissolution of α-V<sub>2</sub>O<sub>5</sub> powder in an aqueous solution containing dopamine ((HO)<sub>2</sub>C<sub>6</sub>H<sub>3</sub>CH<sub>2</sub>CH<sub>2</sub>NH<sub>2</sub>, or Dopa)<sup>24</sup>. The 2D δ-C<sub>x</sub>V<sub>2</sub>O<sub>5</sub>·nH<sub>2</sub>O heterostructure showed significantly improved rate capability and capacity retention compared to pristine δ-V<sub>2</sub>O<sub>5</sub> in nonaqueous Li-ion cells. The positive amine groups in the dopamine molecules could bind to the negative oxide surfaces in the aqueous solution, and the elevated temperatures and pressures attained during the hydrothermal process allowed for dopamine carbonization, resulting in a conductive carbon network. In a separate study, lepidocrocite-type titanium oxide (LTO) and C heterostructures synthesized by annealing selfassembled structures of exfoliated LTO and dopamine exhibited increasing capacity and capacity retention with the increasing content of dopamine-derived carbon<sup>25</sup>. The promise of this strategy was also demonstrated in the MoO<sub>3</sub> system in a study where the hydrothermal treatment of a layered dopamine and molybdenum oxide heterostructure, synthesized through the hydrogen peroxide-assisted oxidation of Mo in a solution containing dopamine as the carbon precursor, led to the formation of an integrated MoO<sub>3</sub>/C electrode material with an improved electronic conductivity and increased charge storage in a 5M ZnCl<sub>2</sub> electrolyte compared to reference α-MoO<sub>3</sub> electrodes<sup>26</sup>. However, cycling instability in the aqueous electrolyte remained an issue, and the amount of charge storage was limited by the electrochemical stability window of the electrolyte.

Another prominent scheme for improving the charge storage properties of  $\alpha$ -MoO<sub>3</sub> is to incorporate oxygen vacancies into the lattice to form a partially reduced MoO<sub>3</sub> structure –  $\alpha$ -MoO<sub>3-x</sub><sup>28-31</sup>. In one study, an  $\alpha$ -MoO<sub>3-x</sub> electrode material that was synthesized through a microwave hydrothermal reaction showed faster charge storage kinetics and better cycling stability than the fully oxidized counterpart in a nonaqueous Li-ion battery<sup>29</sup>. The improved charge storage kinetics and cycling stability were attributed to an increase in the interlayer spacing of  $\alpha$ -MoO<sub>3</sub> and the suppression of irreversible phase transformations upon repeated cycling, respectively, due to the

incorporation of oxygen vacancies in the material's crystal structure. Similar improvements were realized in another study in which  $\alpha$ -MoO<sub>3-x</sub> was synthesized through H<sub>2</sub> plasma etching<sup>30</sup>. Beyond serving as a carbon precursor, dopamine is capable of reducing oxide surfaces, as is required for oxygen vacancy formation<sup>32</sup>; but dopamine has been shown to reduce vanadium and molybdenum oxides to phases where the transition metal is predominantly or completely in a reduced oxidation state when the molecule is incorporated in higher concentrations into the oxides<sup>33, 34</sup>. Contrarily, ethanol has been used as a mild reducing agent to incorporate oxygen vacancies into  $\alpha$ -MoO<sub>3</sub><sup>31</sup>. While the effects of chemically incorporated carbon and oxygen vacancies on the structure and electrochemical properties of  $\alpha$ -MoO<sub>3</sub> have been individually studied, no study on the synergistic effects of chemically incorporated carbon and oxygen vacancies has been performed.

Water-in-salt electrolytes (WISE) that consist of high concentrations of salts dissolved in water have been increasingly examined since their inception as a result of their demonstrated ability to considerably increase the overpotential between the hydrogen and oxygen evolution reactions of water, as well as to suppress parasitic electrode reactions involving water, thereby improving the energy density and cycling stability of aqueous energy storage systems<sup>13, 35-38</sup>. The 30m ZnCl<sub>2</sub> WISE, in particular, was shown in a previous study to improve the rate capability and cycling stability of α-MoO<sub>3</sub> in a Zn/MoO<sub>3</sub> cell compared to equivalent cells with 3M ZnCl<sub>2</sub> and 3M Zn<sub>2</sub>SO<sub>4</sub> electrolytes, where drastic α-MoO<sub>3</sub> capacity fading was witnessed<sup>38</sup>. While the α-MoO<sub>3</sub> electrodes showed promising electrochemistry in water-in-salt energy storage systems, there have been no distinct or combined studies of partially reduced and carbon-containing α-MoO<sub>3</sub> electrode materials in the 30m ZnCl<sub>2</sub> electrolyte.

In this work, the combined effects of dopamine-derived carbon and varying oxygen vacancy concentrations on the structure of α-MoO<sub>3</sub> and the charge transport properties of a produced α-MoO<sub>3-x</sub>/C material in the 30m ZnCl<sub>2</sub> WISE are studied for the first time. Dopamine was integrated with molybdenum oxide through a sol-gel reaction involving the dissolution of Mo in an aqueous solution containing the organic molecule, and dopamine carbonization occurred during a hydrothermal reaction. The oxygen vacancy concentration was tuned by introducing different volumes of ethanol during the hydrothermal treatment process. The WISE allowed for the reversible electrochemical cycling of the electrode materials in a 1.6 V potential window. By analyzing the charge storage kinetics, the charge storage mechanisms, the cycling stability, and

the rate capability of each electrode, the improving effects of dopamine-derived carbon and controlled concentrations of oxygen vacancies are elucidated.

## **Experimental Methods**

# Synthesis of $\alpha$ -MoO<sub>3-x</sub>/C, $\alpha$ -MoO<sub>3-x</sub>/C, $\alpha$ -MoO<sub>3-x</sub>/C-50 $\mu$ L, and $\alpha$ -MoO<sub>3-x</sub>/C-100 $\mu$ L

The MoO<sub>3-x</sub>/C material was synthesized based on a reported sol-gel and hydrothermal treatment reaction<sup>26</sup>. In short, dopamine hydrochloride ((HO)<sub>2</sub>C<sub>6</sub>H<sub>3</sub>CH<sub>2</sub>CH<sub>2</sub>NH<sub>2</sub> HCl, or Dopa HCl, Alfa Aesar) was dissolved in deionized water under magnetic stirring, and molybdenum (Mo) powder (Alfa Aesar) of a stoichiometric amount that corresponded to a Mo:Dopa ratio of 5:1 was subsequently added. Hydrogen peroxide (30 wt% H<sub>2</sub>O<sub>2</sub>, Alfa Aesar) was added dropwise until all Mo dissolved, at which point the reaction temperature was set to 60°C for 18h. The resulting orange gel was freeze-dried (0.001 mbar, -84°C Freezone, Labconco) after overnight freezing at -20°C. The dried powder was added to 12 ml of deionized water in a Teflon-lined autoclave and hydrothermally treated for 24h at 220°C. This product was named ( $\alpha$ /h)-MoO<sub>3-x</sub>/C. The MoO<sub>3-x</sub>/C materials with higher oxygen vacancy concentrations were prepared similarly, but with the addition of 50 µL or 100 µL of ethanol to the autoclave prior to the hydrothermal reaction. Samples resulting from the 50 µL and 100 µL ethanol additions were named  $\alpha$ -MoO<sub>3-x</sub>/C-50µL and  $\alpha$ -MoO<sub>3-x</sub>/C-100µL, respectively. The reference MoO<sub>3</sub> powder was prepared in the absence of Dopa HCl and ethanol, and was named  $\alpha$ -MoO<sub>3</sub>-ref. All reagents were analytical grade and were used without further purification.

#### **Materials Characterization**

Scanning electron microscopy (SEM) images were obtained using a Zeiss Supra 50 VP instrument (Germany). High resolution scanning/transmission electron microscopy (S/TEM) characterization and energy-dispersive X-ray spectroscopy (EDS) mapping were acquired with a FEI Talos F200X analytical S/TEM microscope operated at 200 kV. Micromeritics ASAP 2020 PLUS was used to determine surface area according to the Brunauer–Emmett–Teller (BET) method. All powder materials were degassed at 120 °C for approximately 14 h prior to analysis. To analyze the phase composition of the synthesized materials, X-ray diffraction (XRD) was performed on a Rigaku MiniFlex X-ray diffractometer with Cu Kα radiation. Thermogravimetric analysis (TGA) was conducted in air from room temperature to 700°C using a TA Instruments Q50 (TA Instruments, USA). Raman spectroscopy was performed with a Renishaw inVia Raman microscope using a red 633nm light source. X-ray photoelectron spectroscopy (XPS) measurements were recorded on a Physical Electronics VersaProbe 5000 using a monochromatic

Al K $\alpha$  source and charge compensation. The high-resolution Mo 3d spectra were taken at a pass energy of 23.5 eV with a step size of 0.05 eV. Peak fitting and data analysis were carried out using CasaXPS software. A linear background was used for Mo 3d spectra quantification.

# **Electrochemical Testing and Analysis**

Electrodes with a formulation of 80 wt. % active material, 15 wt. % activated carbon (YP-50, Kuraray Coal<sup>TM</sup>), and 5 wt% poly (tetrafluoroethylene) binder (PTFE, Sigma-Aldrich) were fabricated by mixing the components, in the appropriate ratio, in ethanol at 3,000 rpm using a rotary mixer (FlackTek<sup>TM</sup>), and casting the resulting viscous slurry on carbon paper (AvCarb P50, Fuel Cell Earth) using a blade coater such that the electrode mass loading was regulated between 1.7 and 2.0 mg cm<sup>-2</sup>. Electrochemical data was collected in a two-electrode Swagelok<sup>TM</sup> cell setup, with Zn foil as the counter and reference electrode, glassy carbon as the current collectors, glass fiber (GF/F) as the separator, and 30m ZnCl<sub>2</sub> as the electrolyte. The electrodes were evaluated in a potential window of 0.2 – 1.8 V versus Zn/Zn<sup>2+</sup>, and all potentials were reported with respect to Zn/Zn<sup>2+</sup> reference. Cyclic voltammograms were collected using a BioLogic VP3 potentiostat. Galvanostatic life cycling was performed at a charge/discharge rate of 1,000 mA g<sup>-1</sup> using an Arbin battery testing station. In the rate capability experiments, electrodes were run for ten cycles at the stepwise increased current densities of 200, 500, 1,000, and 2,000 mA g<sup>-1</sup>, and then the current density was brought back down to 200 mA g<sup>-1</sup> to evaluate electrode stability after cycling at high currents.

Cyclic voltammetry analyses were performed to understand the contributions of diffusion-limited and non-diffusion-limited processes to the mechanism of charge storage in the electrodes. The analysis of the current-dependence of the prominent redox features of each electrode material on sweep rate at the peak currents was performed by cycling the electrodes at the sweep rates with 0.2 mV s<sup>-1</sup> increments from 0.2 mV s<sup>-1</sup> to 1.0 mV s<sup>-1</sup>, and modeling the relationship between each peak current and the sweep rate using **Equation 1** that has been found to characterize charge storage processes in electrochemical systems<sup>39, 40</sup>:

$$i = av^b \tag{1}$$

In this equation, i is the peak current, v is the sweep rate, a and b are adjustable parameters related to the charge storage mechanism. A b-value of 0.5 indicates that the current is controlled by diffusion, a b-value of 1.0 indicates a non-diffusion-controlled current response, and

intermediate values signify contributions from both diffusion-controlled and non-diffusion-controlled processes<sup>40</sup>. The b-value was obtained as the slope of a linear fit to the rearranged **Equation 2**:

$$\log(i) = \log(a) + b\log(v) \tag{2}$$

The diffusion-controlled and non-diffusion-controlled contributions to the total capacity of the electrodes at a sweep rate of  $0.5 \text{ mV s}^{-1}$  were evaluated by cycling in  $0.05 \text{ mV s}^{-1}$  increments from  $0.4 \text{ mV s}^{-1}$  to  $0.6 \text{ mV s}^{-1}$ , and decomposing the current responses in the CV data, i(V), at a series of specific potentials into a summation of the diffusion-limited component and the non-diffusion-limited component using **Equation 3**<sup>40,41</sup>:

$$i(V) = k_1 v + k_2 v^{0.5} (3)$$

In this equation, v is the sweep rate, while  $k_1$  and  $k_2$  are coefficients that quantify the non-diffusion-limited contribution and the diffusion-limited contribution, respectively. Relatively slow sweep rates were chosen in both analyses due to the increased limitations of diffusion at higher sweep rates.

#### **Results and Discussion**

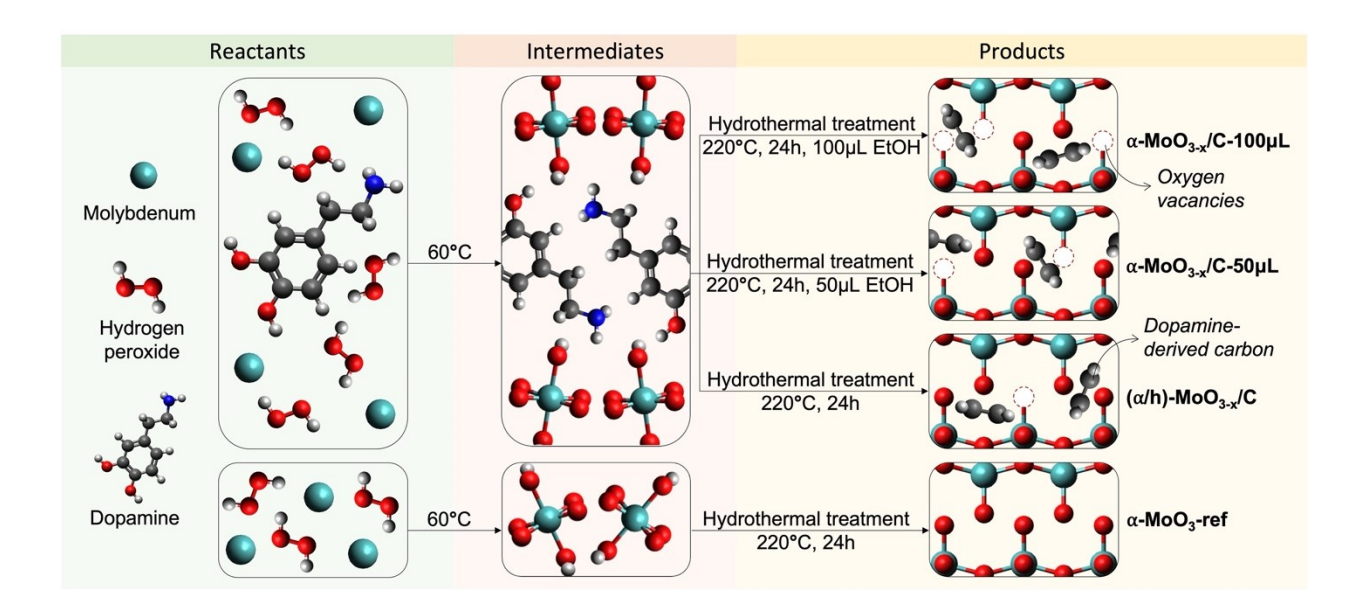


**Figure 1.** Schematic illustration of the approach to synthesizing partially reduced MoO<sub>3</sub> integrated with dopamine-derived carbon and fully oxidized MoO<sub>3</sub>. The products of the sol-gel reaction were freeze-dried and hydrothermally treated. The structure of the final product was determined by the presence (or absence) of dopamine in the sol-gel reaction and ethanol in the hydrothermal reaction.

The strategy adopted for the synthesis of partially reduced MoO<sub>3</sub> integrated with dopamine (Dopa)-derived carbon is shown schematically in **Figure 1**. Temperature elevation to 60°C after the hydrogen peroxide-assisted dissolution of Mo in a dopamine-containing aqueous solution where the Mo:Dopa ratio was 5:1 led to the formation of a Dopa-preintercalated MoO<sub>x</sub> intermediate, as was the case in the previous study<sup>26</sup>. Hydrothermally treating the dried precipitate of this metastable structure for 24h at 220°C in the presence of 0, 50, and 100  $\mu$ L of ethanol resulted in Dopa carbonization and MoO<sub>x</sub> crystallization, yielding integrated MoO<sub>3-x</sub>/C materials (( $\alpha$ /h)-MoO<sub>3-x</sub>/C,  $\alpha$ -MoO<sub>3-x</sub>/C-50 $\mu$ L, and  $\alpha$ -MoO<sub>3-x</sub>/C-100 $\mu$ L, respectively). Layered orthorhombic MoO<sub>3</sub> ( $\alpha$ -MoO<sub>3</sub>-ref) was produced in the absence of dopamine and ethanol. While  $\alpha$ -MoO<sub>3</sub>-ref powders are off-white, ( $\alpha$ /h)-MoO<sub>3-x</sub>/C,  $\alpha$ -MoO<sub>3-x</sub>/C-50 $\mu$ L, and  $\alpha$ -MoO<sub>3-x</sub>/C-100 $\mu$ L powders are blue with the hue deepening towards the latter, which may indicate more oxygen vacancy formation with the darkening of the blue sample color as has been observed in previous studies (**Figure S2, Supporting Information**)<sup>29</sup>.

The morphology of the  $\alpha$ -MoO<sub>3</sub>-ref, ( $\alpha$ /h)-MoO<sub>3-x</sub>/C,  $\alpha$ -MoO<sub>3-x</sub>/C-50 $\mu$ L, and  $\alpha$ -MoO<sub>3-x</sub>/C-100 $\mu$ L particles is shown in **Figure 2**.  $\alpha$ -MoO<sub>3</sub>-ref crystallized as uniform nanobelts with rounded ends (**Figure 2a, b**). ( $\alpha$ /h)-MoO<sub>3-x</sub>/C, which formed when Mo was dissolved in the presence of dopamine and hydrothermal treatment of the resulting intermediate was carried out in the absence of ethanol, also showed a nanobelt morphology (**Figure 2c, d**). However, in comparison to the  $\alpha$ -MoO<sub>3</sub>-ref nanobelts, significant fragmentation of the ( $\alpha$ /h)-MoO<sub>3-x</sub>/C nanobelts is observed. This is consistent with a prior study and is likely attributable to the interactions between interlayer dopamine and MoO<sub>x</sub> layers during the hydrothermal treatment process<sup>26</sup>.

Interestingly, following the addition of 50  $\mu$ L of ethanol to the hydrothermal reaction, the observed morphology changes from nanobelts to a dandelion-like morphology, with one-dimensional particles emerging from a central point to form spherical  $\alpha$ -MoO<sub>3-x</sub>/C-50 $\mu$ L structures (**Figure 2e, f**).  $\alpha$ -MoO<sub>3-x</sub>/C-100 $\mu$ L, the synthesis of which involved 100  $\mu$ L ethanol, also showed a dandelion-like morphology (**Figure 2g, h**); but the ordering of the emergent one-dimensional particles on the surface of the dandelion-like structure is more irregular in  $\alpha$ -MoO<sub>3-x</sub>/C-100 $\mu$ L compared to  $\alpha$ -MoO<sub>3-x</sub>/C-50 $\mu$ L, and the spheres are observed to agglomerate. This greater morphological irregularity observed when the ethanol amount was increased from 50 to 100 uL may be a result of increased interaction between MoO<sub>x</sub>/Dopa and ethanol under the hydrothermal conditions<sup>30</sup>.

The morphology of the synthesized materials was further investigated by TEM analysis. Bright field TEM images under low magnification of the  $\alpha$ -MoO<sub>3</sub>-ref, ( $\alpha$ /h)-MoO<sub>3-x</sub>/C,  $\alpha$ -MoO<sub>3-x</sub>/C-50 $\mu$ L, and  $\alpha$ -MoO<sub>3-x</sub>/C-100 $\mu$ L samples are displayed in **Figure 3a-d**. The  $\alpha$ -MoO<sub>3</sub>-ref and ( $\alpha$ /h)-MoO<sub>3-x</sub>/C materials demonstrated 1D belt-like morphology while  $\alpha$ -MoO<sub>3-x</sub>/C-50 $\mu$ L, and  $\alpha$ -MoO<sub>3-x</sub>/C-100 $\mu$ L samples evinced a bundle-like assembly of thinner nanowires. The average widths of induvial 1D belts/wires are measured to be 175 ± 25 nm, 119 ± 33 nm, 36 ± 10 nm, and 6 ± 2 nm, for  $\alpha$ -MoO<sub>3-x</sub>/C, ( $\alpha$ -MoO<sub>3-x</sub>/C,  $\alpha$ -MoO<sub>3-x</sub>/C-50 $\mu$ L, and  $\alpha$ -MoO<sub>3-x</sub>/C-100 $\mu$ L, respectively. The much thinner nanowire width in  $\alpha$ -MoO<sub>3-x</sub>/C-50 $\mu$ L, and  $\alpha$ -MoO<sub>3-x</sub>/C-100 $\mu$ L samples can contribute to shortened ion-diffusion distance, resulting in enhanced charge transport properties in these two cathodes. High resolution TEM images along with selected area electron diffraction (SAED) patterns of the four samples are depicted in **Figure 3e-h**. The SAED patterns suggest the  $\alpha$ -MoO<sub>3-x</sub>/C-50 $\mu$ L, and  $\alpha$ -MoO<sub>3-x</sub>/C-100 $\mu$ L samples are less crystalline than the  $\alpha$ -MoO<sub>3-x</sub>/C-50 $\mu$ L, and  $\alpha$ -MoO<sub>3-x</sub>/C-samples, possibly due to the incorporation of dopamine-derived

carbon and oxygen vacancies. The lattice fringes in  $\alpha$ -MoO<sub>3-x</sub>/C-100 $\mu$ L sample (**Figure 3h**) are highly discontinuous and mismatched, indicating the dislocations and distortions of the lattice planes due to a defect-rich structure which can in turn tune the resulting electronic properties of the  $\alpha$ -MoO<sub>3-x</sub>/C material. High-angle annular dark-field (HAADF) S/TEM characterizations and EDS mapping of a single belt or bundles are displayed in **Figure S3** (**Supporting Information**). Both Mo and O showed uniform distribution in all four samples while C was only detected in the  $(\alpha/h)$ -MoO<sub>3-x</sub>/C sample. The lack of C signals in  $\alpha$ -MoO<sub>3-x</sub>/C-50 $\mu$ L, and  $\alpha$ -MoO<sub>3-x</sub>/C-100 $\mu$ L samples can be due to the highly localized imaging area. The much higher Mo: O atomic ratio of  $\alpha$ -MoO<sub>3-x</sub>/C-50 $\mu$ L extracted from the EDS maps suggested the presence of oxygen defects in this sample.

The surface areas of the four samples were measured to be 5, 21, 22 and 20 m<sup>2</sup>/g (**Figure S4, Supporting Information**), for the  $\alpha$ -MoO<sub>3</sub>-ref, ( $\alpha$ /h)-MoO<sub>3-x</sub>/C,  $\alpha$ -MoO<sub>3-x</sub>/C-50 $\mu$ L, and  $\alpha$ -MoO<sub>3-x</sub>/C-100 $\mu$ L samples, respectively. The incorporation of dopamine with or without ethanol into the synthesis route significantly increased the surface area when compared with the reference material, in part due to the decreased nanobelt width and the presence of surface defects.

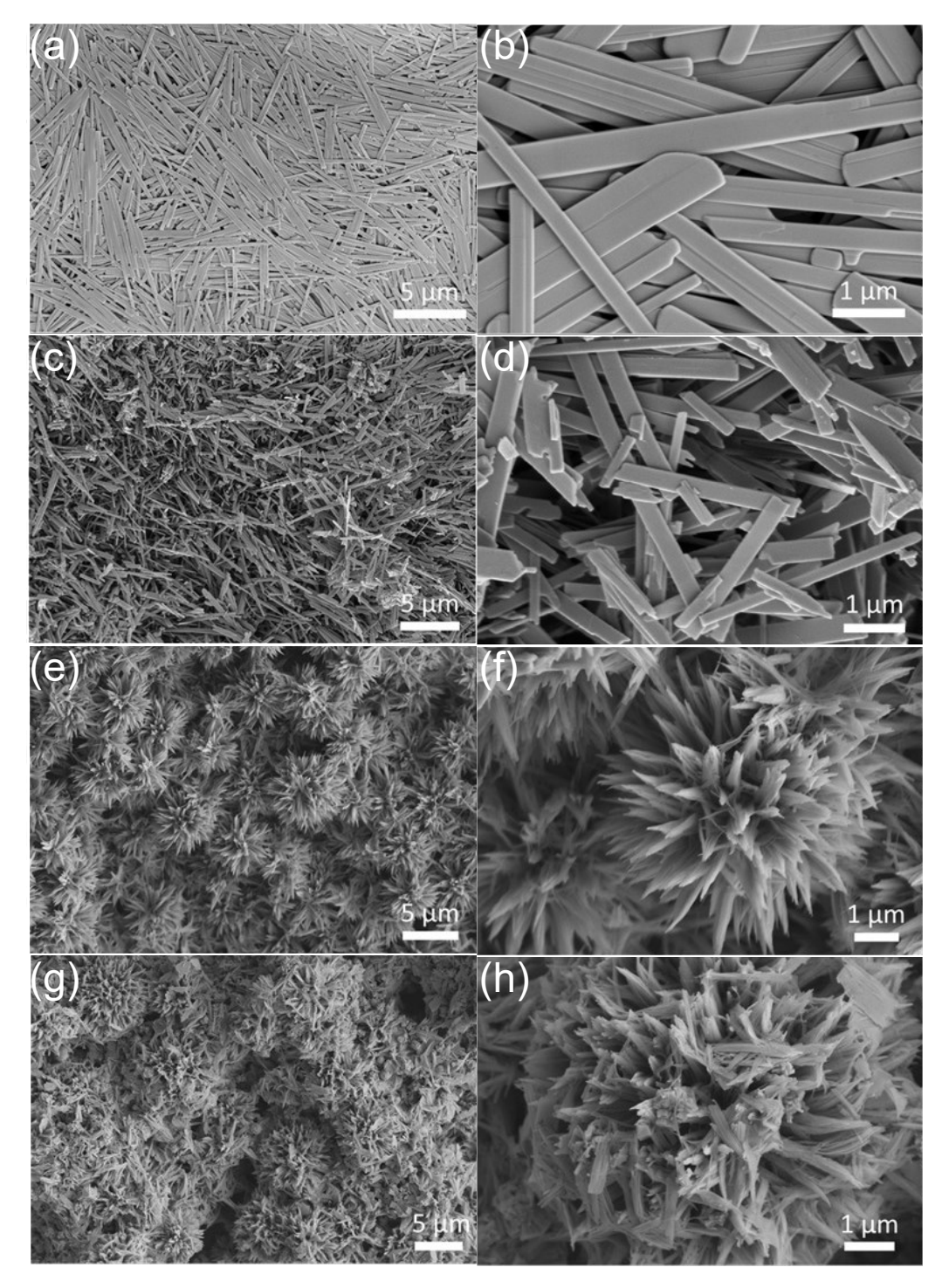


**Figure 2.** SEM images of (a, b)  $\alpha$ -MoO<sub>3</sub>-ref, (c, d) ( $\alpha$ /h)-MoO<sub>3-x</sub>/C, (e, f)  $\alpha$ -MoO<sub>3-x</sub>/C-50 $\mu$ L, and (g, h)  $\alpha$ -MoO<sub>3-x</sub>/C-100 $\mu$ L. (a, c, e, g) Low- and (b, d, f, h) high-magnification images are shown.

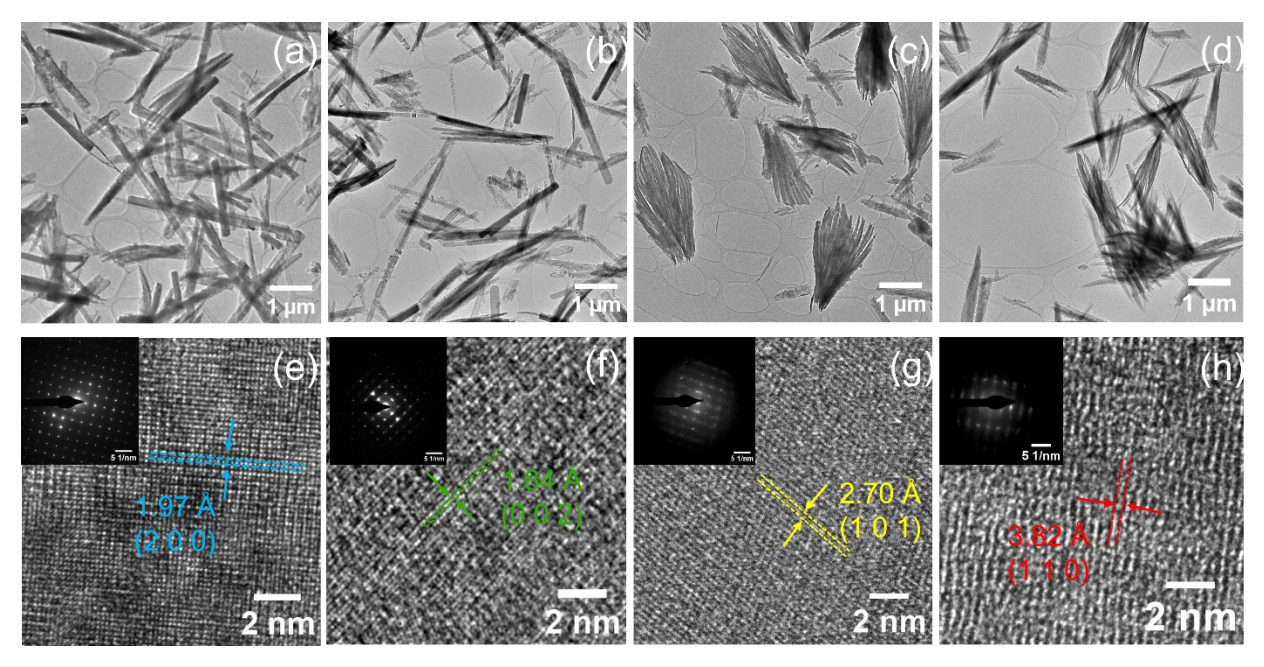


**Figure 3**. Low magnification TEM images (a-d), HRTEM images and SAED patterns (inset) (e-h) of the as-prepared α-MoO<sub>3</sub>-ref, (α/h)-MoO<sub>3-x</sub>/C, α-MoO<sub>3-x</sub>/C-50μL, and α-MoO<sub>3-x</sub>/C-100μL materials.

The X-ray diffractograms of the synthesized materials are shown in Figure 4a. The crystal structure of α-MoO<sub>3</sub>-ref corresponds to that of the orthorhombic MoO<sub>3</sub> phase (α-MoO<sub>3</sub>, JCPDS No. 05-0508) in the *Pbnm* space group. The  $\alpha$ -MoO<sub>3</sub>-ref diffractogram shows intense (0k0) reflections, likely indicating texturing due to preferred crystal growth in the b direction. Although the  $\alpha$ -MoO<sub>3</sub> phase is dominant in the  $(\alpha/h)$ -MoO<sub>3-x</sub>/C sample, additional weak reflections, such as that at 9.9°, are observed, indicating the partial formation of a secondary crystal structure. In the previous study, it was found that these reflections can be indexed with the hexagonal MoO<sub>3</sub> phase (h-MoO<sub>3</sub>)<sup>16, 26</sup>. However, the h-MoO<sub>3</sub> phase is not observed in the diffractograms of the materials synthesized in the presence of ethanol during hydrothermal treatment. The major reflections in XRD patterns of  $\alpha$ -MoO<sub>3-x</sub>/C-50 $\mu$ L and  $\alpha$ -MoO<sub>3-x</sub>/C-100 $\mu$ L can be indexed to the  $\alpha$ -MoO<sub>3</sub> phase. The d-spacing of the (020) planes was calculated from the position of the (020) peak in the  $\alpha$ -MoO<sub>3</sub> XRD signal and showed increases from 6.69 Å in α-MoO<sub>3</sub>-ref, to 6.85 Å in (α/h)-MoO<sub>3</sub>- $_{\rm x}/{\rm C}$ , and to 6.93 Å in  $\alpha$ -MoO<sub>3-x</sub>/C-50 $\mu$ L and  $\alpha$ -MoO<sub>3-x</sub>/C-100 $\mu$ L (Figure S5, Supporting **Information**). These expansions in the  $\alpha$ -MoO<sub>3</sub> b lattice parameter could be attributed to the formation of oxygen vacancies, in agreement with the sample color change and previous studies<sup>29</sup>, <sup>30</sup>. Increased α-MoO<sub>3</sub> interlayer spacings due to oxygen vacancy formation have been correlated

with improvements in the material's ionic conductivity and the facilitated diffusion of electrochemically cycled ions through the material, leading in turn to enhanced charge storage kinetics<sup>29, 30</sup>. While the crystal structures of  $\alpha$ -MoO<sub>3-x</sub>/C-50 $\mu$ L and  $\alpha$ -MoO<sub>3-x</sub>/C-100 $\mu$ L are characterized by identical (020) *d*-spacings, interplanar ordering in  $\alpha$ -MoO<sub>3-x</sub>/C-100 $\mu$ L is comparatively lower, as indicated by the wider full width at half maximum of its counterpart (020) reflection (**Figure S5, Supporting Information**). This corroborates the increased morphological irregularity observed in the SEM images of  $\alpha$ -MoO<sub>3-x</sub>/C-100 $\mu$ L compared to those of  $\alpha$ -MoO<sub>3-x</sub>/C-50 $\mu$ L.

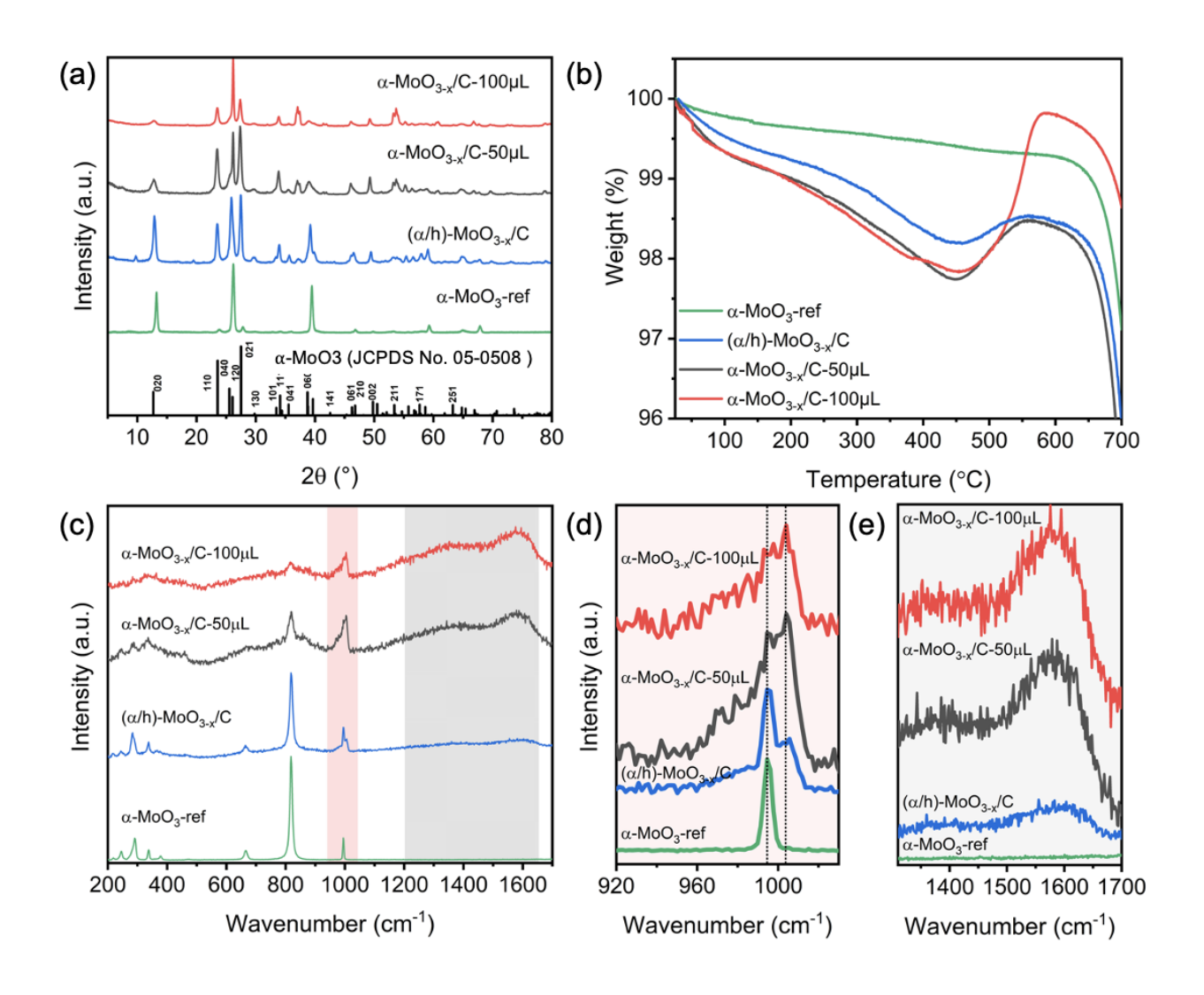


**Figure 4.** Structural and thermal characterization of α-MoO<sub>3</sub>-ref, (α/h)-MoO<sub>3-x</sub>/C, α-MoO<sub>3-x</sub>/C-50μL, and α-MoO<sub>3-x</sub>/C-100μL: (a) XRD patterns, (b) TGA weight loss curves, (c) Raman spectra, and (d, e) selected regions in Raman spectra corresponding to (d) bands indicative of oxygen vacancies and (e) carbon bands. The spectra shown in (d) and (e) are colored light red and light grey, respectively, in accordance with the corresponding regions highlighted in (c).

The results of TGA measurements are presented in **Figure 4b**. The upper temperature limit was set at 700°C because MoO<sub>3</sub> sublimes above this temperature.  $\alpha$ -MoO<sub>3</sub>-ref shows a slight weight loss up to 600°C, which can be attributed to the loss of adsorbed water and low fractions of structural water. ( $\alpha$ /h)-MoO<sub>3-x</sub>/C and  $\alpha$ -MoO<sub>3-x</sub>/C-50 $\mu$ L undergo similar patterns of weight loss. Both materials lose a higher percentage of mass than  $\alpha$ -MoO<sub>3</sub>-ref up to 600°C, likely due to water evolution processes and the decomposition of carbonized dopamine. Additionally, both materials show a gain in mass between 450°C and 550°C, with the percentage increase being comparatively

higher for  $\alpha$ -MoO<sub>3-x</sub>/C-50 $\mu$ L. Even greater weight gains occur in  $\alpha$ -MoO<sub>3-x</sub>/C-100 $\mu$ L. This phenomenon can be ascribed to the oxidation of partially reduced MoO<sub>3</sub> in air and is consistent with prior studies<sup>26, 42, 43</sup>. The results suggest not only that hydrothermal treatment in the presence of ethanol leads to the formation of oxygen vacancies in MoO<sub>3</sub> due to the action of ethanol as a reducing agent, but also that dopamine reduces MoO<sub>3</sub> and contributes to oxygen vacancy formation.

Raman spectroscopy measurements are displayed in **Figure 4c**. Characteristic  $\alpha$ -MoO<sub>3</sub> vibrations appear at 993, 818, 663, 377, 336, 292 and 244 cm<sup>-1</sup> <sup>44-46</sup>; but the peaks broaden in the order of  $\alpha$ -MoO<sub>3-ref</sub>, ( $\alpha$ /h)-MoO<sub>3-x</sub>/C,  $\alpha$ -MoO<sub>3-x</sub>/C-50 $\mu$ L, and  $\alpha$ -MoO<sub>3-x</sub>/C-100 $\mu$ L, indicating a wider distribution of local environments, likely due to the introduction of structural defects. The 993 cm<sup>-1</sup> peak that is present in the spectrum of each material arises due to the stretching of terminal Mo=O bonds<sup>44-46</sup>. However, in addition to this vibration, a new vibration with a peak at 1004 cm<sup>-1</sup> is observed in the spectra of ( $\alpha$ /h)-MoO<sub>3-x</sub>/C,  $\alpha$ -MoO<sub>3-x</sub>/C-50 $\mu$ L, and  $\alpha$ -MoO<sub>3-x</sub>/C-100 $\mu$ L (**Figure 4d**). The intensity of the 1004 cm<sup>-1</sup> peak relative to the 993 cm<sup>-1</sup> peak increases from the former material to the latter. Prior studies have assigned this peak to the emergent antisymmetric stretching of the terminal Mo=O as a result of the presence of oxygen vacancies and have correlated the broadening and intensifying of this peak with increases in oxygen vacancy concentration<sup>30, 45, 46</sup>. These spectroscopic results are, therefore, in agreement with conclusions based on TGA experiments. ( $\alpha$ /h)-MoO<sub>3-x</sub>/C,  $\alpha$ -MoO<sub>3-x</sub>/C-50 $\mu$ L, and  $\alpha$ -MoO<sub>3-x</sub>/C-100 $\mu$ L also show the characteristic D and G bands of carbon near 1400 and 1600 cm<sup>-1</sup>, respectively, thus confirming the integration of carbon into the structures (**Figure 4e**)<sup>26, 47</sup>.

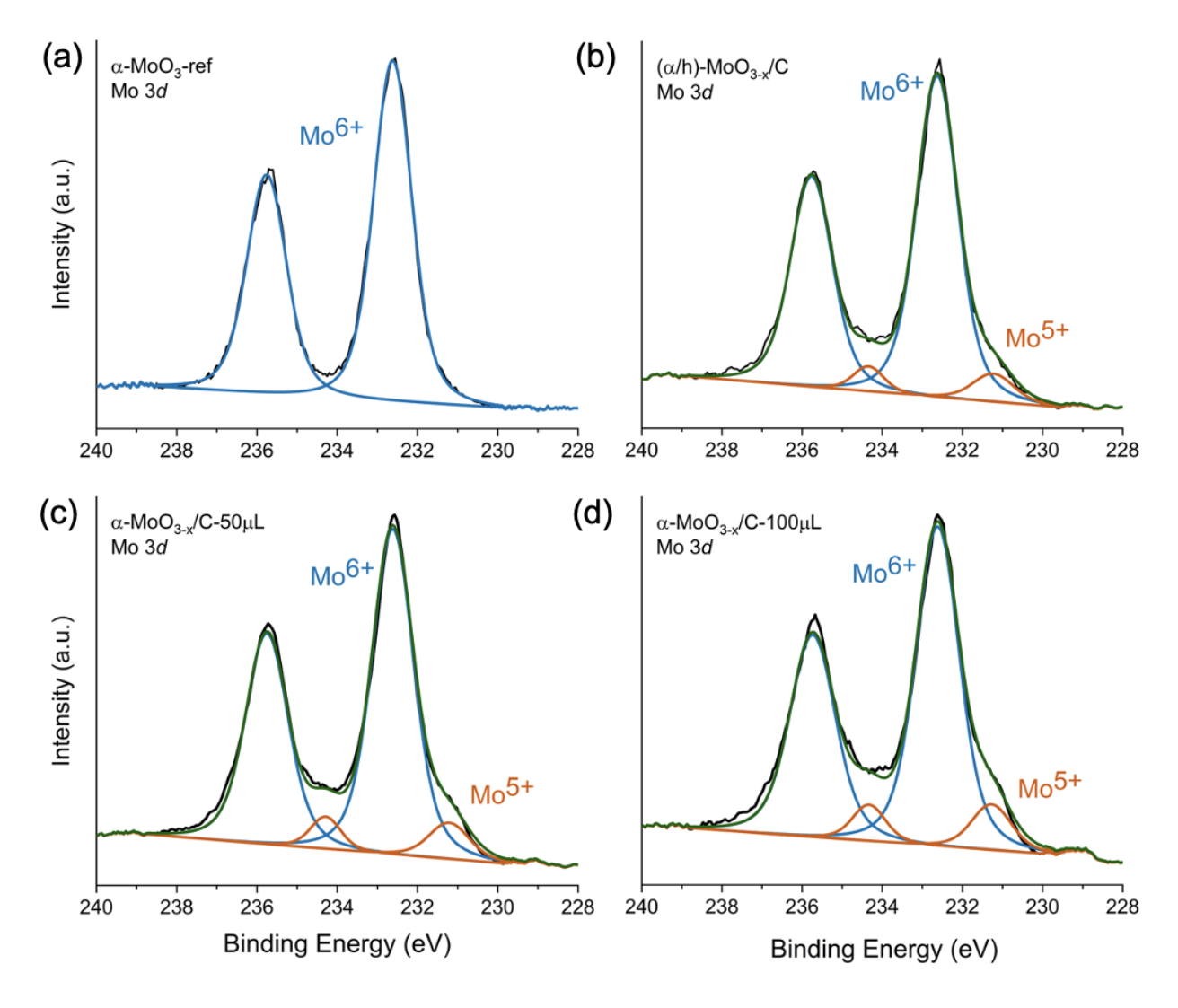


**Figure 5.** XPS spectra of the Mo 3*d* region for (a)  $\alpha$ -MoO<sub>3</sub>-ref, (b) ( $\alpha$ /h)-MoO<sub>3-x</sub>/C, (c)  $\alpha$ -MoO<sub>3-x</sub>/C-50 $\mu$ L, and (d)  $\alpha$ -MoO<sub>3-x</sub>/C-100 $\mu$ L.

**Table 1.** Summary table of Mo *3d* XPS data.

	Mo 3d oxidation state (at %) (BE (eV))	
Sample	<i>Mo</i> <sup>6+</sup> (232.6)	$Mo^{5+}(231.2)$
α-MoO <sub>3</sub> -Ref	100	0
$(\alpha/h)$ - $MoO_{3-x}/C$	92	8
$\alpha$ -MoO <sub>3-x</sub> /C-50 $\mu$ L	90	10
$\alpha$ -MoO <sub>3-x</sub> /C-100 $\mu$ L	88	12

Mo 3d XPS spectra were acquired to compare the oxygen vacancy concentrations in  $\alpha$ -MoO<sub>3</sub>-ref,  $(\alpha/h)$ -MoO<sub>3-x</sub>/C,  $\alpha$ -MoO<sub>3-x</sub>/C-50 $\mu$ L, and  $\alpha$ -MoO<sub>3-x</sub>/C-100 $\mu$ L (Figure 5). While  $\alpha$ -MoO<sub>3</sub>-ref only shows peaks corresponding to Mo<sup>6+</sup> ions,  $(\alpha/h)$ -MoO<sub>3-x</sub>/C,  $\alpha$ -MoO<sub>3-x</sub>/C-50 $\mu$ L, and α-MoO<sub>3-x</sub>/C-100μL show peaks at lower binding energies attributable to Mo<sup>5+</sup> ions. Using similar XPS characterization approaches as well as density functional theory (DFT)-based calculations, previous studies have demonstrated that the stable configuration of oxygen vacancies in MoO<sub>3-x</sub> entails the presence of  $Mo^{+5}$  ions at the defect center<sup>29, 30</sup>. The presence of  $Mo^{5+}$  ions in  $(\alpha/h)$ - $MoO_{3-x}/C$ ,  $\alpha$ - $MoO_{3-x}/C$ - $50\mu$ L, and  $\alpha$ - $MoO_{3-x}/C$ - $100\mu$ L may therefore be attributed to the formation of oxygen vacancies in these materials due to the reducing effects of dopamine and ethanol when incorporated into the hydrothermal reaction, in agreement with Raman spectroscopy and TGA measurements, as well as the color changes of the samples. The estimated atomic percentages of Mo<sup>6+</sup> and Mo<sup>5+</sup> ions in each material are listed in **Table 1**. A trend is observed where the materials prepared in the presence of dopamine and increasing volumes of ethanol exhibit a higher degree of reduction from Mo<sup>6+</sup> to Mo<sup>5+</sup>. The fractions of Mo<sup>5+</sup> in α-MoO<sub>3</sub>-ref,  $(\alpha/h)-MoO_{3-x}/C$ ,  $\alpha-MoO_{3-x}/C-50\mu L$ , and  $\alpha-MoO_{3-x}/C-100\mu L$  are 0, 8, 10, and 12 at. %, respectively. Formation of oxygen vacancies was further confirmed by analyzing the O 1s XPS spectra of the synthesized materials (Figure S6 and Table S1 in Supporting Information).

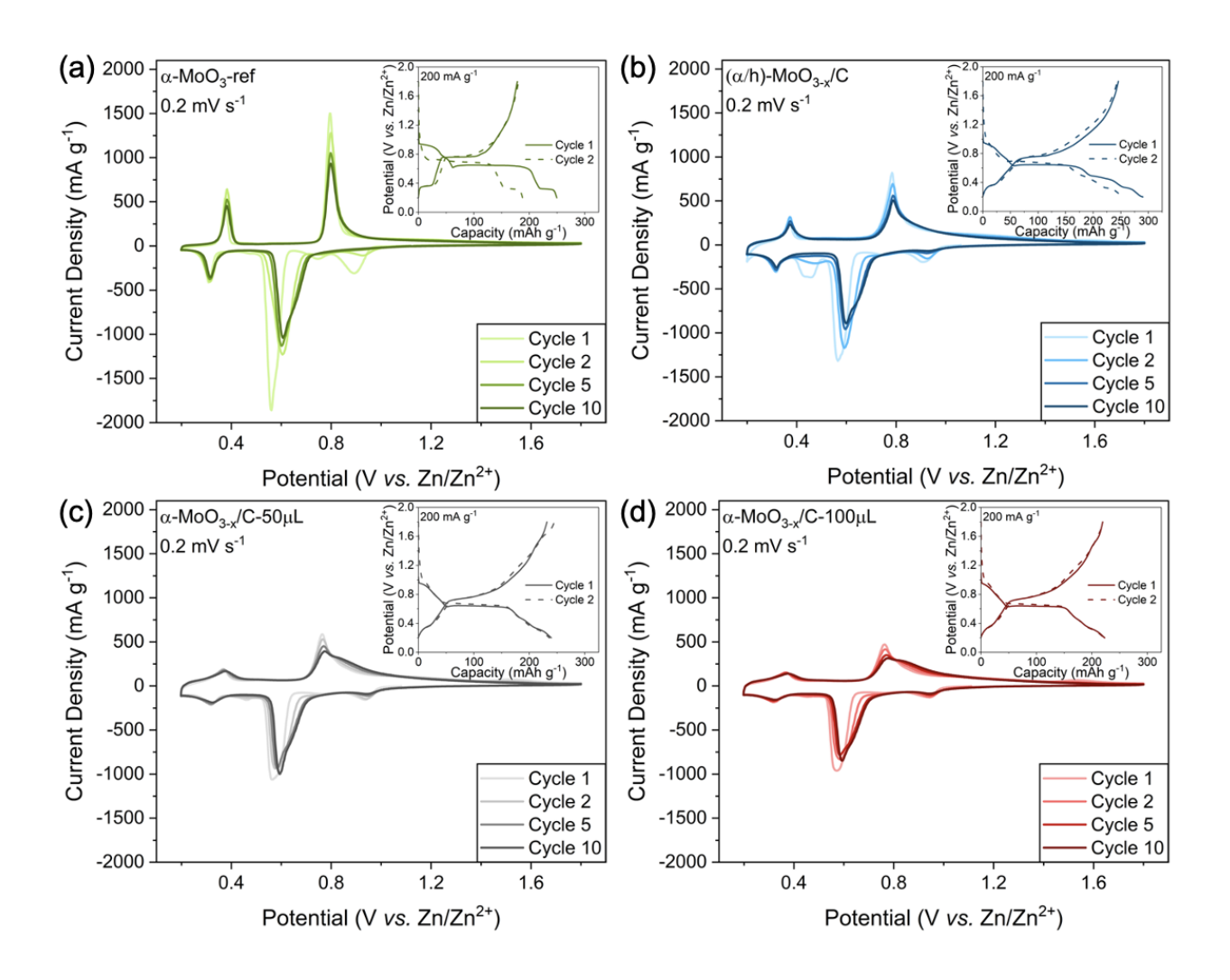


**Figure 6.** Cyclic voltammetry profiles of the first ten cycles at 0.2 mV s<sup>-1</sup> exhibited by Zn-ion WISE cells containing (a) α-MoO<sub>3</sub>-ref, (b) (α/h)-MoO<sub>3-x</sub>/C, (c) α-MoO<sub>3-x</sub>/C-50μL, and (d) α-MoO<sub>3-x</sub>/C-100μL electrodes. Insets show corresponding 1<sup>st</sup> and 2<sup>nd</sup> cycle galvanostatic discharge/charge curves at 200 mA g<sup>-1</sup>.

To assess the charge storage characteristics of  $\alpha$ -MoO<sub>3-x</sub>/C-50 $\mu$ L and  $\alpha$ -MoO<sub>3-x</sub>/C-100 $\mu$ L in comparison to ( $\alpha$ /h)-MoO<sub>3-x</sub>/C and  $\alpha$ -MoO<sub>3</sub>-ref, cyclic voltammetry (CV) experiments were performed at 0.2 mV s<sup>-1</sup> in a 0.2 – 1.8V vs Zn/Zn<sup>2+</sup> potential window and in a 30m ZnCl<sub>2</sub> electrolyte. **Figure 6** shows the 1<sup>st</sup>, 2<sup>nd</sup>, 5<sup>th</sup>, and 10<sup>th</sup> cycle CV curves of the electrode materials, and **Figure S7** (**Supporting Information**) shows the overlaid cyclic voltammetry curves of the electrode materials after 10 cycles. During the first cathodic sweep (discharge step) under this set of conditions, the  $\alpha$ -MoO<sub>3</sub>-ref electrode (**Figure 6a**) shows two irreversible deposition processes at 0.90 V and 0.75 V, in addition to prominent redox processes at 0.59 V and 0.32 V with

corresponding processes at 0.79 V and 0.38 V during the anodic sweep (charge step). However, during the subsequent discharge step, the peak at 0.59 V substantially diminishes, broadens, and shifts to higher potentials, likely signifying a modification of the initial charge storage site due to the cycling-induced irreversible transformation and degradation of the pristine structure<sup>38, 48</sup>. The peak at 0.79 V during the charge step is also observed to progressively fade. The galvanostatic discharge/charge curves of  $\alpha$ -MoO<sub>3</sub>-ref at 200 mA g<sup>-1</sup> are consistent with this behavior, with the discharge capacity dropping significantly from 249 mAh g<sup>-1</sup> to 188 mAh g<sup>-1</sup> (76% retention) between the first and second cycles.

The  $(\alpha/h)$ -MoO<sub>3-x</sub>/C electrode features two redox couples at potentials similar to those at which similar features are observed in the  $\alpha$ -MoO<sub>3</sub>-ref electrode, but significant variations in the charge storage behavior and new sites of electrochemical activity are observed (Figure 6b). Firstly, the current densities associated with the redox peaks in the  $(\alpha/h)$ -MoO<sub>3-x</sub>/C electrodes are reduced, but a wider rectangular envelope predominantly between 0.2 and 1.2 V is observed. This potentially indicates a suppression of the irreversible charge storage reactions occurring at these potentials in α-MoO<sub>3</sub>-ref during the initial cycles, accompanied by an increase in potentialindependent charge storage due to the incorporation of dopamine-derived carbon and oxygen vacancies, as shown through the structural characterization highlighted hitherto. Secondly, the irreversible first-cycle discharge process appearing at 0.75 V in α-MoO<sub>3</sub>-ref is inhibited, and the reversibility of the peak at 0.90 V is improved. The latter process persists up to the 10<sup>th</sup> cycle. Finally, uniquely to this electrode, a pair of peaks centered at 0.48 V during the first discharge step is noted, although it fades during subsequent cycles. In a previous study, charge storage in  $(\alpha/h)$ -MoO<sub>3-x</sub>/C in a 5M ZnCl<sub>2</sub> electrolyte occurred in sites that were absent or electrochemically inactive in α-MoO<sub>3</sub>-ref<sup>26</sup>. This phenomenon was attributed to the improved electron transfer capability of  $(\alpha/h)$ -MoO<sub>3-x</sub>/C compared to  $\alpha$ -MoO<sub>3</sub>-ref due to the presence of an intimate MoO<sub>3</sub>/C heterointerface, the results of which were enhanced charge transfer, and ultimately, an increase in charge storage capacity. Herein, (α/h)-MoO<sub>3-x</sub>/C exhibits not only a higher initial capacity compared to α-MoO<sub>3</sub>-ref in the 30m ZnCl<sub>2</sub> WISE, but also improved capacity retention between the first and second cycles. As displayed in the corresponding galvanostatic discharge/charge profiles, an initial discharge capacity of 290 mAh g<sup>-1</sup> is attained at 200 mA g<sup>-1</sup>, and 253 mAh g<sup>-1</sup> (87%) is retained on the second discharge cycle at this current density.

Compared to  $(\alpha/h)$ -MoO<sub>3-x</sub>/C, the first-cycle cyclic voltammetry profile of the  $\alpha$ -MoO<sub>3-x</sub> <sub>x</sub>/C-50μL electrode is characterized by analogous redox peaks occurring at the same potentials and a substantial rectangular envelope (Figure 6c). Nevertheless, distinguishing characteristics are also apparent. The irreversible peaks near 0.48 V during the discharge steps in  $(\alpha/h)$ -MoO<sub>3-x</sub>/C are inhibited in  $\alpha$ -MoO<sub>3-x</sub>/C-50 $\mu$ L, the reversibility of the peak at 0.60 V is further improved, and the specific currents associated with the prominent redox couples during the first cycle are further reduced. Of particular note is that upon continuous cycling, a peak at 0.85 V during charge steps evolves, while the peak at 0.76 V diminishes. The absence of this new peak in α-MoO<sub>3</sub>-ref and  $(\alpha/h)$ -MoO<sub>3-x</sub>/C suggests that it is linked to the presence of an increased concentration of oxygen vacancies. It has been discovered that the breakage of crystal symmetry in MoO<sub>3</sub> due to the incorporation of oxygen vacancies can result in the splitting of the energies associated with charge storage sites, leading to the observance of peaks at higher potentials<sup>29</sup>. The evolution of the peak in α-MoO<sub>3-x</sub>/C-50μL may suggest an energetic preference for charge storage at this site. The inset shows that at 200 mA g<sup>-1</sup>, the first-cycle discharge capacity of α-MoO<sub>3-x</sub>/C-50μL is 240 mAh g<sup>-1</sup>. While this is lower than the initial capacity of (α/h)-MoO<sub>3-x</sub>/C, 238 mAh g<sup>-1</sup> (99%) is retained on the second cycle – a 12% increase in capacity retention compared to  $(\alpha/h)$ -MoO<sub>3-x</sub>/C and a 23% increase compared to  $\alpha$ -MoO<sub>3</sub>-ref. The lower initial capacity of  $\alpha$ -MoO<sub>3-x</sub>/C-50 $\mu$ L may therefore originate from the mitigation of irreversible reactions during its first cycle. These observations indicate that the presence of a higher concentration of oxygen vacancies in the crystal structure of α-MoO<sub>3</sub> can produce advancements in cycling stability. This apparently holds valid when considering the α-MoO<sub>3-x</sub>/C-100µL electrodes, whose first-cycle cyclic voltammetry profile closely resembles that of the α-MoO<sub>3-x</sub>/C-50μL electrodes, and which also demonstrates a capacity retention of 99% between its first and second cycles at 200 mA g<sup>-1</sup>. However, α-MoO<sub>3-x</sub>/C-100μL exhibits a lower first cycle discharge capacity (223 mAh g<sup>-1</sup>) than α-MoO<sub>3-x</sub>/C-50μL in the galvanostatic discharge/charge experiments, thus indicating that the presence of high oxygen vacancy concentrations in MoO<sub>3</sub> can distort the structure of the lattice such that charge storage sites are rendered inaccessible. A similar phenomenon was observed in the study of MoO<sub>3-x</sub> synthesized through plasma etching<sup>30</sup>. Tuning the oxygen vacancy concentration, as is done in this work using ethanol as a reducing agent during a hydrothermal treatment procedure, is therefore nontrivial in optimizing the electrochemical properties of MoO<sub>3-x</sub>/C. Beyond this, excessive

ethanol reduction of MoO<sub>3</sub> leads to the formation of MoO<sub>2</sub> (**Figure S8** in **Supporting Information**).

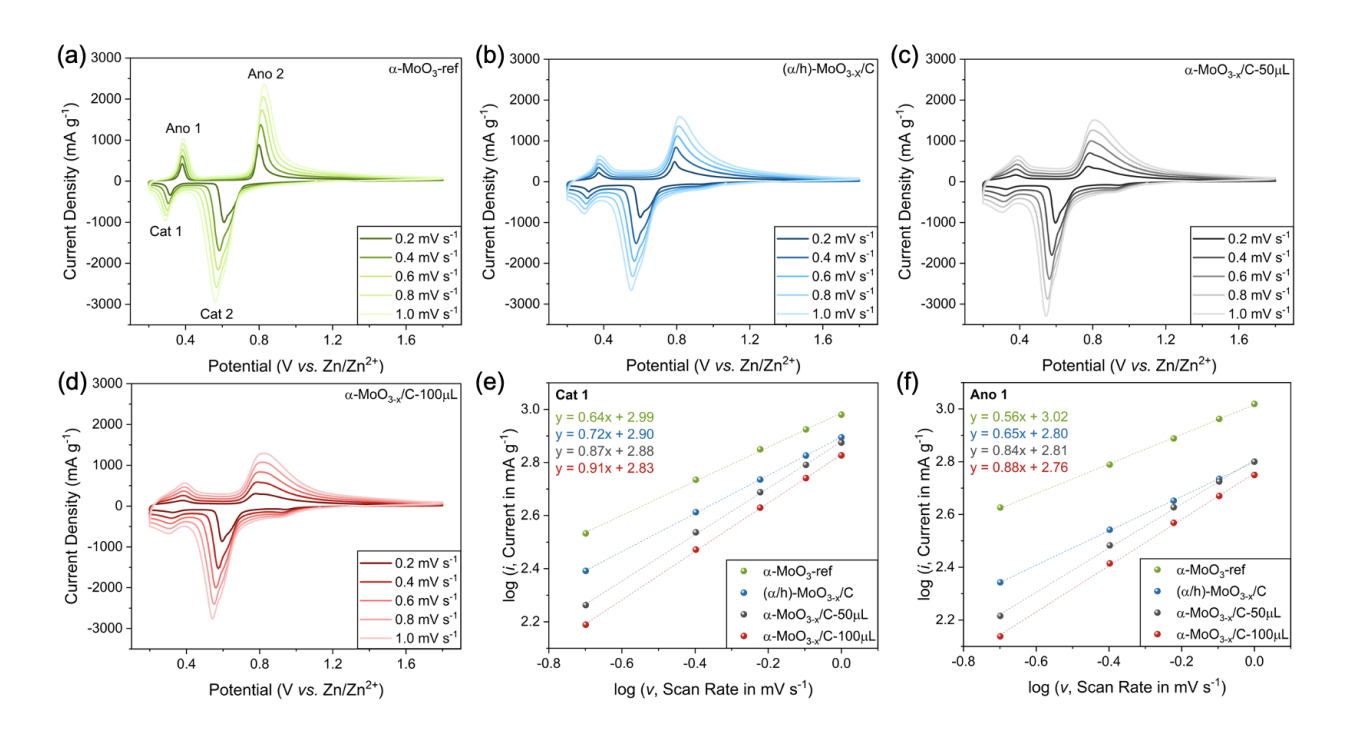


**Figure 7.** Cyclic voltammetry profiles of the Zn-ion WISE cells containing (a) α-MoO<sub>3</sub>-ref, (b)  $(\alpha/h)$ -MoO<sub>3-x</sub>/C, (c) α-MoO<sub>3-x</sub>/C-50μL, and (d) α-MoO<sub>3-x</sub>/C-100μL electrodes at 0.2, 0.4, 0.6, 0.8, and 1.0 mV s<sup>-1</sup>. Log(*i*) versus log(*v*) plots of (e) Cat 1 and (f) Ano 1 as defined in (a).

To understand the differences in the kinetics of charge transport in  $\alpha$ -MoO<sub>3</sub>-ref, ( $\alpha$ /h)-MoO<sub>3-x</sub>/C,  $\alpha$ -MoO<sub>3-x</sub>/C-50 $\mu$ L, and  $\alpha$ -MoO<sub>3-x</sub>/C-100 $\mu$ L, the respective electrodes were cycled from 0.2 to 1.0 mV s<sup>-1</sup> in increments of 0.2 mV s<sup>-1</sup> (**Figure 7a–d**). The charge storage behaviors of each electrode are generally retained at the increased scan rates, as is indicated by the similarity between the higher and lower rate profiles. However, the overpotential between the redox processes increases as the scan rate increases, indicating an increasing limitation of charge storage due to diffusion of the electrochemically cycled species through the electrode materials. The mechanisms of charge storage at the prominent redox potentials were evaluated by analyzing the dependence of the currents at the peak potentials on scan rate. The plots of log (i) against log (v) for the cathodic currents at approximately 0.3 V and 0.6 V, as well as the anodic currents at approximately 0.4 V and 0.8 V (Cat 1, Cat 2, Ano 1, and Ano 2, respectively, as defined in **Figure 6a**) are presented in **Figures 7e**, **7f**, **S9a**, **and S9b**. The Cat 1 and Ano 1 b-values were determined to be

0.64 and 0.56 in the  $\alpha$ -MoO<sub>3</sub>-ref electrodes, 0.72 and 0.65 in the ( $\alpha$ /h)-MoO<sub>3-x</sub>/C electrodes, 0.87 and 0.84 in the  $\alpha$ -MoO<sub>3-x</sub>/C-50 $\mu$ L electrodes, and 0.91 and 0.88 in the  $\alpha$ -MoO<sub>3-x</sub>/C-100 $\mu$ L electrodes, respectively. This implies that as carbon and increasing concentrations of oxygen vacancies are incorporated into MoO<sub>3</sub>, the currents associated with these features are increasingly dominated by rapid, non-diffusion-limited processes as opposed to sluggish, diffusion-limited processes. Cat 2 and Ano 2 show the same general behavior, despite the similarity between the *b*-values associated with Cat 2 in the  $\alpha$ -MoO<sub>3-x</sub>/C-50 $\mu$ L and  $\alpha$ -MoO<sub>3-x</sub>/C-100 $\mu$ L electrodes.

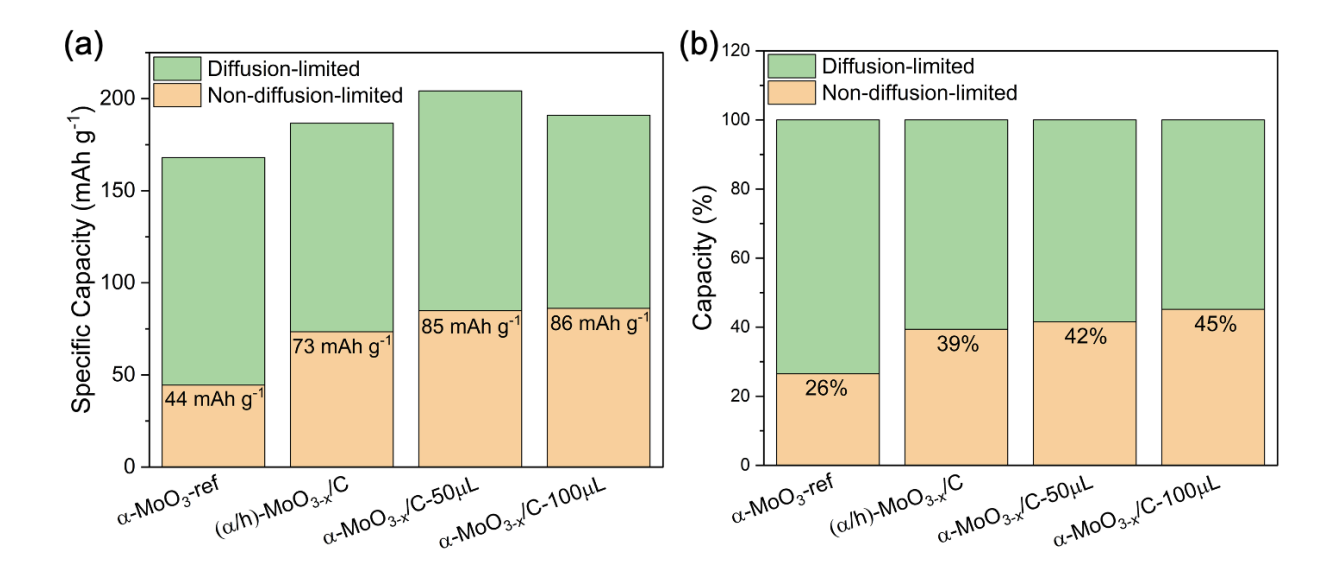


**Figure 8.** Diffusion-limited and non-diffusion limited contributions to the discharge capacity of α-MoO<sub>3</sub>-ref, (α/h)-MoO<sub>3-x</sub>/C, α-MoO<sub>3-x</sub>/C-50μL, and α-MoO<sub>3-x</sub>/C-100μL electrodes in Zn-ion WISE cells at 0.5 mV s<sup>-1</sup>. Capacity is expressed in (a) mAh g<sup>-1</sup> and (b) percentage (%).

The increased level of non-diffusion-limited charge storage in the MoO<sub>3-x</sub>/C electrodes has been further demonstrated by analyzing the contributions of distinct diffusion-limited and non-diffusion-limited charge storage processes to the total capacity of the electrodes at specific scan rates. The relative contributions to the discharge capacity of  $\alpha$ -MoO<sub>3-ref</sub>,  $(\alpha/h)$ -MoO<sub>3-x</sub>/C,  $\alpha$ -MoO<sub>3-x</sub>/C-50 $\mu$ L, and  $\alpha$ -MoO<sub>3-x</sub>/C-100 $\mu$ L at 0.5 mV s<sup>-1</sup> are highlighted in **Figure 8**. The amount of the discharge capacity stemming from rapid, non-diffusion-limited processes increases from 44 mAh g<sup>-1</sup> (26 %) in  $\alpha$ -MoO<sub>3-ref</sub>, to 73 mAh g<sup>-1</sup> (39 %) in  $(\alpha/h)$ -MoO<sub>3-x</sub>/C, to 85 mAh g<sup>-1</sup> (42 %) in  $\alpha$ -MoO<sub>3-x</sub>/C-50 $\mu$ L, and to 86 mAh g<sup>-1</sup> (46 %) in  $\alpha$ -MoO<sub>3-x</sub>/C-100 $\mu$ L. Total discharge capacity also increases between  $\alpha$ -MoO<sub>3</sub>-ref and  $\alpha$ -MoO<sub>3-x</sub>/C-50 $\mu$ L, but in consistency with the galvanostatic

discharge/charge curves at 200 mA g<sup>-1</sup>,  $\alpha$ -MoO<sub>3-x</sub>/C-100 $\mu$ L delivers a lower capacity than  $\alpha$ -MoO<sub>3-x</sub>/C-50 $\mu$ L. These results clearly show that chemically incorporating dopamine-derived carbon and oxygen vacancies into the structure of  $\alpha$ -MoO<sub>3</sub> leads to facilitated charge transport through the material. The advancements correlate with increases in electronic conductivity measured using a four-point probe method (**Table S2** in **Supporting Information**) and expansions of the interlayer spacing measured through XRD, the latter of which is beneficial for ionic conductivity. Nevertheless, the introduction of high vacancy concentrations can hinder charge storage.

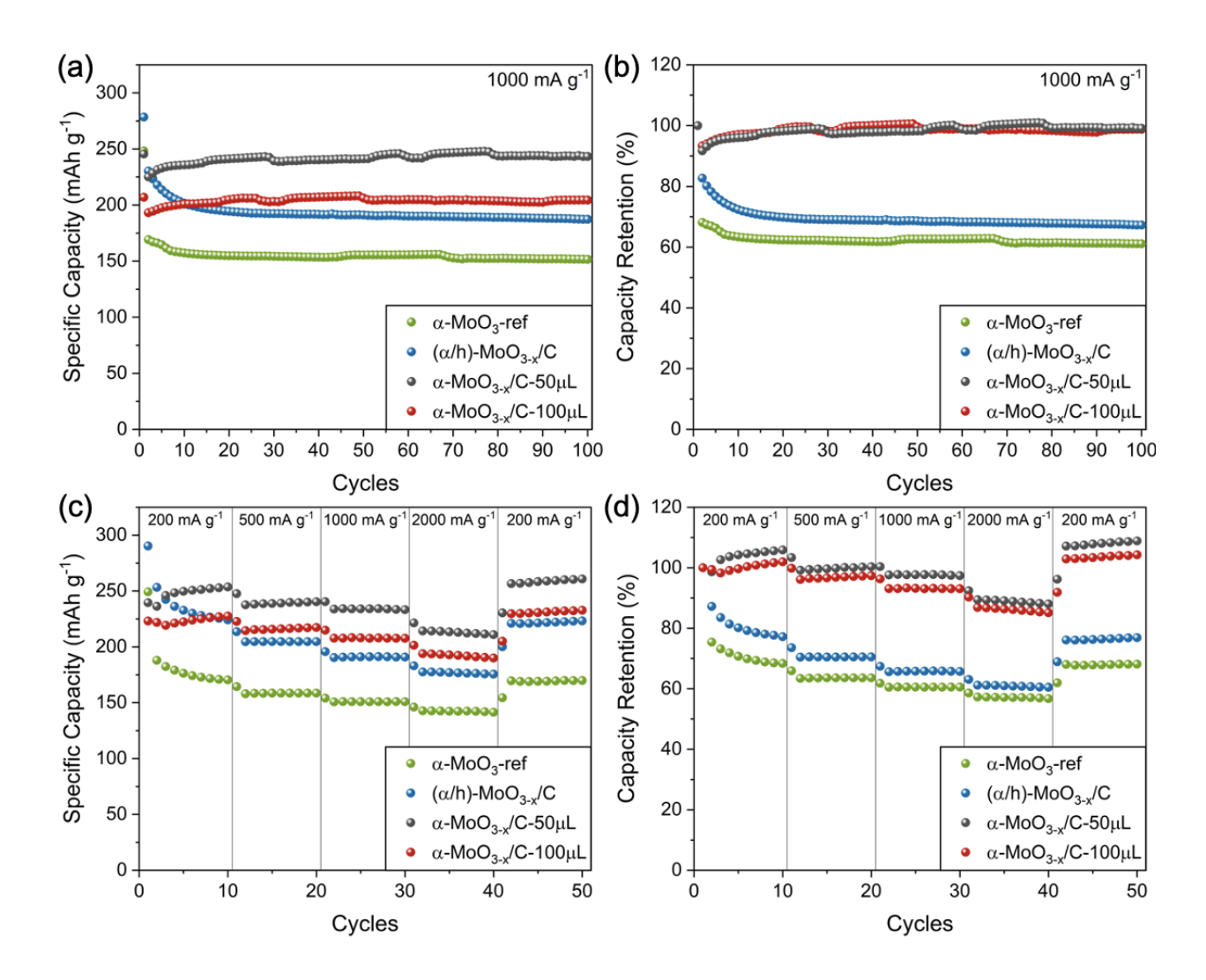


**Figure 9.** (a, b) Extended cycling at a current density of 1000 mA g<sup>-1</sup> and (c, d) rate capability experiment consisting of ten cycles each at a current density of 200, 500, 1000, 2000, and 200 mA g<sup>-1</sup> of the Zn-ion WISE cells containing α-MoO<sub>3</sub>-ref, (α/h)-MoO<sub>3-x</sub>/C, α-MoO<sub>3-x</sub>/C-50μL, and α-MoO<sub>3-x</sub>/C-100μL electrodes. (a, c) Discharge capacities and (b, d) capacity retentions.

Considering the positive effects of carbon and oxygen vacancies on the kinetics of charge transport and storage in  $\alpha$ -MoO<sub>3</sub>, the cycling stability of the electrodes was evaluated at 1,000 mA g<sup>-1</sup> (**Figure 9a, b**). The discharge and charge profiles of the electrodes during the 1<sup>st</sup> and the 100<sup>th</sup> cycles are presented in **Figure S10** (**Supporting Information**). After 100 cycles, the  $\alpha$ -MoO<sub>3-r</sub>/C,  $\alpha$ -MoO<sub>3-x</sub>/C-50 $\mu$ L, and  $\alpha$ -MoO<sub>3-x</sub>/C-100 $\mu$ L electrodes deliver 152, 187, 243, and 204 mAh g<sup>-1</sup>, respectively, corresponding to 61, 67, 99, and 99 % discharge capacity retentions, respectively. Interestingly, the  $\alpha$ -MoO<sub>3-x</sub>/C-50 $\mu$ L and  $\alpha$ -MoO<sub>3-x</sub>/C-100 $\mu$ L electrodes undergo capacity increases between the 2<sup>nd</sup> and the 20<sup>th</sup> cycles. This could be due to a combination of the low cycling-induced capacity decay as well as the time-dependent wetting of the electrodes by the viscous 30m ZnCl<sub>2</sub> WISE<sup>38</sup>. It is likely that capacity increases resulting from this wetting phenomenon are not evident in  $\alpha$ -MoO<sub>3</sub>-ref and ( $\alpha$ /h)-MoO<sub>3-x</sub>/C due to the simultaneously occurring capacity decreases of these materials during cycling.

The results of rate capability experiments are shown in **Figure 9 c, d**. The discharge and charge profiles of the electrodes on the second cycle at each current density are presented in **Figure S11 (Supporting Information)**. All electrode materials show over 90% discharge capacity retention between the final cycle at each rate and the second cycle at the subsequent rate between 200 and 2000 mA g<sup>-1</sup> (**Table S3** in **Supporting Information**). Additionally, all electrode materials show over 99% discharge capacity retention between cycle 10, the last cycle at the initial 200 mA g<sup>-1</sup> rate, and cycle 42, the second cycle after returning to 200 mA g<sup>-1</sup>. This indicates an impressive tolerance to high currents, due in part to the stabilizing effect of the 30m ZnCl<sub>2</sub> WISE<sup>38, 49</sup>. The highly saturated electrolyte can suppress the dissolution of MoO<sub>3</sub>, which is known to be one of the mechanisms leading to the capacity decay in this material. Furthermore, the dopamine-derived carbon may play a role in suppressing dissolution. If carbon is present at the electrode/electrolyte interface, MoO<sub>3</sub> is less exposed to the electrolyte, and dissolution is hindered. If carbon is in the interlayer region, the top MoO<sub>3</sub> layer may dissolve, but this would again lead to the presence of interfacial carbon that protects MoO<sub>3</sub> underneath from continued dissolution.

At higher current densities, the MoO<sub>3-x</sub>/C electrodes deliver superior discharge capacities. On the second cycle at 500, 1,000, and 2,000 mA g<sup>-1</sup>,  $\alpha$ -MoO<sub>3</sub>-ref delivers 158, 151, and 143 mAh g<sup>-1</sup>;  $(\alpha/h)$ -MoO<sub>3-x</sub>/C delivers 205, 190, and 178 mAh g<sup>-1</sup>;  $\alpha$ -MoO<sub>3-x</sub>/C-100 $\mu$ L delivers 215, 208, and 193 mAh g<sup>-1</sup>; and  $\alpha$ -MoO<sub>3-x</sub>/C-50 $\mu$ L delivers the highest capacities of 237, 234, and 214 mAh g<sup>-1</sup>; respectively. Moreover, the  $\alpha$ -MoO<sub>3-x</sub>/C-50 $\mu$ L electrodes show a 9% capacity increase

between the first and fiftieth cycles in the rate capability experiment, compared to a slightly lower increase of 4% in the  $\alpha$ -MoO<sub>3-x</sub>/C-100 $\mu$ L electrodes, a 23% decrease in the ( $\alpha$ /h)-MoO<sub>3-x</sub>/C electrodes, and a 32% decrease in the  $\alpha$ -MoO<sub>3</sub>-ref electrodes. The outstanding performance of  $\alpha$ -MoO<sub>3-x</sub>/C-50 $\mu$ L at high current densities attests to the positive effects of chemically introduced dopamine-derived carbon and controlled concentrations of oxygen vacancies on the electrochemical properties of  $\alpha$ -MoO<sub>3</sub>. This superiority of  $\alpha$ -MoO<sub>3-x</sub>/C-50 $\mu$ L and  $\alpha$ -MoO<sub>3-x</sub>/C-100 $\mu$ L electrodes compared to  $\alpha$ -MoO<sub>3</sub>-ref and ( $\alpha$ /h)-MoO<sub>3-x</sub>/C is also evident when the materials are evaluated as active materials in binder-free electrodes with carbon nanotubes as the conductive additive, Zn foil as the counter electrode, and 30m ZnCl<sub>2</sub> as the electrolyte (**Figure S12** in **Supporting Information**). Carbon improves the charge transfer capability of the material by enhancing electronic conductivity, while oxygen vacancies improve ionic conductivity and facilitate the suppression of irreversible reactions and structural transformations that hinder cycling stability. These improved charge transport properties enable rapid charge storage in the 30m ZnCl<sub>2</sub> WISE.

#### **Conclusions**

The synergistic effects of synthetically incorporated carbon and oxygen vacancies on the charge storage properties of α-MoO<sub>3</sub> in a 30m ZnCl<sub>2</sub> water-in-salt electrolyte have been examined in this work. A tight MoO<sub>3</sub>/carbon heterointerface was created through chemical preintercalation of dopamine molecules followed by carbonization, while formation of oxygen vacancies in MoO<sub>3</sub> was achieved via addition of ethanol during a hydrothermal treatment synthesis step. TGA, Raman spectroscopy, and XPS measurements indicate that the oxygen vacancy concentration increases with the increasing content of ethanol in the hydrothermal reaction, and that dopamine carbonization in the absence of ethanol is associated with minute oxygen vacancy formation. XRD patterns show that the vdW gap in MoO<sub>3</sub> structure also generally increases with increasing oxygen vacancy concentration.

The kinetics of charge storage increase, with  $\alpha$ -MoO<sub>3-x</sub>/C-50 $\mu$ L and  $\alpha$ -MoO<sub>3-x</sub>/C-100 $\mu$ L exhibiting the highest fractions of non-diffusion-limited charge storage mechanisms at 0.5 mV s<sup>-1</sup>. These advancements correlate with expanded interlayer spacings and higher four-point probe electronic conductivity values. Oxygen vacancies within the Mo-O layer could create pathways for electrochemically cycled ions to diffuse not only through the interlayer region but also across

stacked structural layers in the MoO<sub>3</sub> structure, thus leading to enhanced ion conductivity and overall enhanced charge storage properties. However, control of the oxygen vacancy concentration is critical, as  $\alpha$ -MoO<sub>3-x</sub>/C-100 $\mu$ L exhibits lower capacities than  $\alpha$ -MoO<sub>3-x</sub>/C-50 $\mu$ L. After 100 cycles at 1,000 mA g<sup>-1</sup>, the  $\alpha$ -MoO<sub>3-x</sub>/C-50 $\mu$ L electrode delivers a discharge capacity of 243 mAh g<sup>-1</sup>, corresponding to a 99% capacity retention. In contrast,  $\alpha$ -MoO<sub>3</sub>-ref, the reference  $\alpha$ -MoO<sub>3</sub> electrode material, delivers a discharge capacity of 152 mAh g<sup>-1</sup> (61% retention) after 100 cycles at this current density. At 2,000 mA g<sup>-1</sup>,  $\alpha$ -MoO<sub>3-x</sub>/C-50 $\mu$ L delivers a discharge capacity of up to 214 mAh g<sup>-1</sup>, while  $\alpha$ -MoO<sub>3</sub>-ref delivers 143 mAh g<sup>-1</sup>. The respectable performance of  $\alpha$ -MoO<sub>3</sub>-ref at these high current densities attests to the stabilizing effect of the 30m ZnCl<sub>2</sub> WISE, but the superior performance of  $\alpha$ -MoO<sub>3-x</sub>/C-50 $\mu$ L proves that incorporating carbon and moderate concentrations of oxygen vacancies into  $\alpha$ -MoO<sub>3</sub>, as is performed in this work, is a promising strategy to realize improvements in charge storage kinetics, cycling stability, and rate capability. Prospectively, the principles herein established can be used to enhance the energy storage characteristics of other metal oxide systems.

# Acknowledgements

This work was supported as part of the Center for Mesoscale Transport Properties, an Energy Frontier Research Center supported by the U.S. Department of Energy, Office of Science, Basic Energy Sciences via grant #DE-SC0012673. The scanning transmission electron microscopy measurements used resources of the Center for Functional Nanomaterials, which is a U.S. DOE Office of Science Facility, at Brookhaven National Laboratory under Contract No. DE-SC0012704. XPS and Raman spectroscopy characterization was supported by the National Science Foundation under Grant No. DMR-1752623. We also thank Drexel's Materials Characterization Core (MCC) facility for providing access to characterization instruments. EST acknowledges the William and Jane Knapp Chair of Energy and the Environment.

#### References

- (1) Pomerantseva, E.; Bonaccorso, F.; Feng, X.; Cui, Y.; Gogotsi, Y. Energy storage: The future enabled by nanomaterials. *Science (American Association for the Advancement of Science)* **2019**, *366* (6468), 969. DOI: 10.1126/science.aan8285.
- (2) Gür, T. M. Review of electrical energy storage technologies, materials and systems: challenges and prospects for large-scale grid storage. *Energy & environmental science* **2018**, *11* (1), 2696-2767. DOI: 10.1039/c8ee01419a.
- (3) Doughty, D. H.; Roth, E. P. A General Discussion of Li Ion Battery Safety. *The Electrochemical Society interface* **2012**, *21* (2), 37-44. DOI: 10.1149/2.F03122if.
- (4) Liu, K.; Liu, Y.; Lin, D.; Pei, A.; Cui, Y. Materials for lithium-ion battery safety. *Science Advances* **2018**, *4* (6), eaas9820-eaas9820. DOI: 10.1126/sciadv.aas9820.
- (5) Wang, Q.; Ping, P.; Zhao, X.; Chu, G.; Sun, J.; Chen, C. Thermal runaway caused fire and explosion of lithium ion battery. *Journal of power sources* **2012**, *208*, 210-224. DOI: 10.1016/j.jpowsour.2012.02.038.
- (6) Bandhauer, T. M.; Garimella, S.; Fuller, T. F. A Critical Review of Thermal Issues in Lithium-Ion Batteries. *Journal of the Electrochemical Society* **2011**, *158* (3), R1. DOI: 10.1149/1.3515880.
- (7) Liu, J.; Xu, C.; Chen, Z.; Ni, S.; Shen, Z. X. Progress in aqueous rechargeable batteries. *Green Energy & Environment* **2018**, *3* (1), 20-41. DOI: 10.1016/j.gee.2017.10.001.
- (8) Chao, D.; Zhou, W.; Xie, F.; Ye, C.; Li, H.; Jaroniec, M.; Qiao, S.-Z. Roadmap for advanced aqueous batteries: From design of materials to applications. *Science advances* **2020**, *6* (21), eaba4098-eaba4098. DOI: 10.1126/sciadv.aba4098.
- (9) Chang, Z.; Yang, Y.; Li, M.; Wang, X.; Wu, Y. Green energy storage chemistries based on neutral aqueous electrolytes. *Journal of materials chemistry. A, Materials for energy and sustainability* **2014**, *2* (28), 10739-10755. DOI: 10.1039/C4TA00565A.

- (10) Han, C.; Li, W.; Liu, H. K.; Dou, S.; Wang, J. Principals and strategies for constructing a highly reversible zinc metal anode in aqueous batteries. *Nano energy* **2020**, *74*, 104880. DOI: 10.1016/j.nanoen.2020.104880.
- (11) Hu, L.; Xiao, P.; Xue, L.; Li, H.; Zhai, T. The rising zinc anodes for high-energy aqueous batteries. *EnergyChem* **2021**, *3* (2), 100052. DOI: 10.1016/j.enchem.2021.100052.
- (12) Song, M.; Tan, H.; Chao, D.; Fan, H. J. Recent Advances in Zn-Ion Batteries. *Advanced functional materials* **2018**, *28* (41), 1802564-n/a. DOI: 10.1002/adfm.201802564.
- (13) Zhang, C.; Holoubek, J.; Wu, X.; Daniyar, A.; Zhu, L.; Chen, C.; Leonard, D. P.; Rodríguez-Pérez, I. A.; Jiang, J.-X.; Fang, C.; et al. A ZnCl2 water-in-salt electrolyte for a reversible Zn metal anode. *Chemical communications (Cambridge, England)* **2018**, *54* (100), 14097-14099. DOI: 10.1039/c8cc07730d.
- (14) Tang, K.; Farooqi, S. A.; Wang, X.; Yan, C. Recent Progress on Molybdenum Oxides for Rechargeable Batteries. *ChemSusChem* **2019**, *12* (4), 755-771. DOI: 10.1002/cssc.201801860.
- (15) Chernova, N. A.; Roppolo, M.; Dillon, A. C.; Whittingham, M. S. Layered vanadium and molybdenum oxides: batteries and electrochromics. *Journal of materials chemistry* **2009**, *19* (17), 2526-2552. DOI: 10.1039/b819629j.
- (16) Chithambararaj, A.; Rajeswari Yogamalar, N.; Bose, A. C. Hydrothermally Synthesized h-MoO3 and α-MoO3 Nanocrystals: New Findings on Crystal-Structure-Dependent Charge Transport. *Crystal growth & design* **2016**, *16* (4), 1984-1995. DOI: 10.1021/acs.cgd.5b01571.
- (17) Yang, W.; Xiao, J.; Ma, Y.; Cui, S.; Zhang, P.; Zhai, P.; Meng, L.; Wang, X.; Wei, Y.; Du, Z.; et al. Tin Intercalated Ultrathin MoO3 Nanoribbons for Advanced Lithium–Sulfur Batteries. *Advanced energy materials* **2019**, *9* (7), n/a. DOI: 10.1002/aenm.201803137.
- (18) Mai, L. Q.; Hu, B.; Chen, W.; Qi, Y. Y.; Lao, C. S.; Yang, R. S.; Dai, Y.; Wang, Z. L. Lithiated MoO3 Nanobelts with Greatly Improved Performance for Lithium Batteries. *Advanced materials (Weinheim)* **2007**, *19* (21), 3712-3716. DOI: 10.1002/adma.200700883.

- (19) Elkholy, A. E.; Duignan, T. T.; Sun, X.; Zhao, X. S. Stable α-MoO3 Electrode with a Widened Electrochemical Potential Window for Aqueous Electrochemical Capacitors. *ACS applied energy materials* **2021**, *4* (4), 3210-3220. DOI: 10.1021/acsaem.0c02990.
- (20) de Castro, I. A.; Datta, R. S.; Ou, J. Z.; Castellanos-Gomez, A.; Sriram, S.; Daeneke, T.; Kalantar-zadeh, K. Molybdenum Oxides From Fundamentals to Functionality. *Advanced materials (Weinheim)* **2017**, *29* (40), 1701619-n/a. DOI: 10.1002/adma.201701619.
- (21) Boyd, S.; Augustyn, V. Transition metal oxides for aqueous sodium-ion electrochemical energy storage. *Inorganic chemistry frontiers* **2018**, *5* (5), 999-115. DOI: 10.1039/c8qi00148k.
- (22) Yang, L.; Kong, J.; Zhou, D.; Ang, J. M.; Phua, S. L.; Yee, W. A.; Liu, H.; Huang, Y.; Lu, X. Transition-Metal-Ion-Mediated Polymerization of Dopamine: Mussel-Inspired Approach for the Facile Synthesis of Robust Transition-Metal Nanoparticle—Graphene Hybrids. *Chemistry—A European Journal* **2014**, *20* (25), 7776-7783.
- (23) Zhao, C.; Wang, X.; Kong, J.; Ang, J. M.; Lee, P. S.; Liu, Z.; Lu, X. Self-assembly-induced alternately stacked single-layer MoS2 and N-doped graphene: A novel van der Waals heterostructure for lithium-ion batteries. *ACS applied materials & interfaces* **2016**, *8* (3), 2372-2379.
- (24) Clites, M.; Andris, R.; Cullen, D. A.; More, K. L.; Pomerantseva, E. Improving Electronic Conductivity of Layered Oxides through the Formation of Two-Dimensional Heterointerface for Intercalation Batteries. *ACS applied energy materials* **2020**, *3* (4), 3835-3844. DOI: 10.1021/acsaem.0c00274.
- (25) Barim, G.; Dhall, R.; Arca, E.; Kuykendall, T. R.; Yin, W.; Takeuchi, K. J.; Takeuchi, E. S.; Marschilok, A. C.; Doeff, M. M. Heterostructured Lepidocrocite Titanate-Carbon Nanosheets for Electrochemical Applications. *ACS applied nano materials* **2022**, *5* (1), 678-690. DOI: 10.1021/acsanm.1c03449.
- (26) Norouzi, N.; Omo-Lamai, D.; Alimohammadi, F.; Averianov, T.; Kuang, J.; Yan, S.; Wang, L.; Stavitski, E.; Leshchev, D.; Takeuchi, K. J.; et al. The Dopamine Assisted Synthesis of

- MoO3/Carbon Electrodes With Enhanced Capacitance in Aqueous Electrolyte. *Frontiers in chemistry* **2022**, *10*, 873462-873462. DOI: 10.3389/fchem.2022.873462.
- (27) Pomerantseva, E. Chemical preintercalation synthesis of versatile electrode materials for electrochemical energy storage. *Accounts of Chemical Research* **2022**, *56* (1), 13-24.
- (28) Xiao, X.; Peng, Z.; Chen, C.; Zhang, C.; Beidaghi, M.; Yang, Z.; Wu, N.; Huang, Y.; Miao, L.; Gogotsi, Y. Freestanding MoO3– x nanobelt/carbon nanotube films for Li-ion intercalation pseudocapacitors. *Nano Energy* **2014**, *9*, 355-363.
- (29) Kim, H.-S.; Cook, J. B.; Lin, H.; Ko, Jesse S.; Tolbert, Sarah H.; Ozolins, V.; Dunn, B. Oxygen vacancies enhance pseudocapacitive charge storage properties of MoO3–x. *Nature materials* **2017**, *16* (4), 454-460. DOI: 10.1038/nmat4810.
- (30) Zhang, G.; Xiong, T.; Yan, M.; He, L.; Liao, X.; He, C.; Yin, C.; Zhang, H.; Mai, L. α-MoO3- by plasma etching with improved capacity and stabilized structure for lithium storage. *Nano energy* **2018**, *49*, 555-563. DOI: 10.1016/j.nanoen.2018.04.075.
- (31) Zheng, W.; Halim, J.; Etman, A. S.; El Ghazaly, A.; Rosen, J.; Barsoum, M. W. Boosting the volumetric capacitance of MoO3-x free-standing films with Ti3C2 MXene. *Electrochimica Acta* **2021**, *370*, 137665.
- (32) Xu, L. Q.; Yang, W. J.; Neoh, K.-G.; Kang, E.-T.; Fu, G. D. Dopamine-induced reduction and functionalization of graphene oxide nanosheets. *Macromolecules* **2010**, *43* (20), 8336-8339.
- (33) Andris, R.; Averianov, T.; Pomerantseva, E. Phase transformation and electrochemical charge storage properties of vanadium oxide/carbon composite electrodes synthesized via integration with dopamine. *Journal of the American Ceramic Society* **2022**.
- (34) Norouzi, N.; Averianov, T.; Kuang, J.; Bock, D.; Yan, S.; Wang, L.; Takeuchi, K.; Takeuchi, E.; Marschilok, A.; Pomerantseva, E. Hierarchically structured MoO2/dopamine-derived carbon spheres as intercalation electrodes for lithium-ion batteries. *Materials Today Chemistry* **2022**, *24*, 100783.

- (35) Suo, L.; Borodin, O.; Gao, T.; Olguin, M.; Ho, J.; Fan, X.; Luo, C.; Wang, C.; Xu, K. "Water-in-salt" electrolyte enables high-voltage aqueous lithium-ion chemistries. *Science* **2015**, *350* (6263), 938-943.
- (36) Shen, Y.; Liu, B.; Liu, X.; Liu, J.; Ding, J.; Zhong, C.; Hu, W. Water-in-salt electrolyte for safe and high-energy aqueous battery. *Energy Storage Materials* **2021**, *34*, 461-474.
- (37) Saraf, M.; Shuck, C. E.; Norouzi, N.; Matthews, K.; Inman, A.; Zhang, T.; Pomerantseva, E.; Gogotsi, Y. Free-Standing α-MoO3/Ti3C2 MXene Hybrid Electrode in Water-in-Salt Electrolytes. *Energy & Environmental Materials*, e12516.
- (38) Wang, L.; Yan, S.; Quilty, C. D.; Kuang, J.; Dunkin, M. R.; Ehrlich, S. N.; Ma, L.; Takeuchi, K. J.; Takeuchi, E. S.; Marschilok, A. C. Achieving Stable Molybdenum Oxide Cathodes for Aqueous Zinc-Ion Batteries in Water-in-Salt Electrolyte. *Advanced materials interfaces* **2021**, *8* (9), 2002080-n/a. DOI: 10.1002/admi.202002080.
- (39) Lindström, H.; Södergren, S.; Solbrand, A.; Rensmo, H.; Hjelm, J.; Hagfeldt, A.; Lindquist, S.-E. Li+ Ion Insertion in TiO2 (Anatase). 2. Voltammetry on Nanoporous Films. *JOURNAL OF PHYSICAL CHEMISTRY B* **1997**, *101* (39), 7717-7722. DOI: 10.1021/jp970490q.
- (40) Wang, J.; Polleux, J.; Lim, J.; Dunn, B. Pseudocapacitive Contributions to Electrochemical Energy Storage in TiO2 (Anatase) Nanoparticles. *Journal of physical chemistry. C* **2007**, *111* (40), 14925-14931. DOI: 10.1021/jp074464w.
- (41) Brezesinski, T.; Wang, J.; Tolbert, S. H.; Dunn, B. Ordered mesoporous alpha-MoO3 with iso-oriented nanocrystalline walls for thin-film pseudocapacitors. *Nature materials* **2010**, *9* (2), 146-151. DOI: 10.1038/nmat2612.
- (42) Yazdani, S.; Kashfi-Sadabad, R.; Huan, T. D.; Morales-Acosta, M. D.; Pettes, M. T. Polyelectrolyte-Assisted Oxygen Vacancies: A New Route to Defect Engineering in Molybdenum Oxide. *Langmuir* **2018**, *34* (21), 6296-6306. DOI: 10.1021/acs.langmuir.8b00539.
- (43) Wu, D.; Shen, R.; Yang, R.; Ji, W.; Jiang, M.; Ding, W.; Peng, L. Mixed Molybdenum Oxides with Superior Performances as an Advanced Anode Material for Lithium-Ion Batteries. *Scientific Reports* **2017**, *7* (1), 44697-44697. DOI: 10.1038/srep44697.

- (44) Mestl, G.; Ruiz, P.; Delmon, B.; Knozinger, H. Oxygen-Exchange Properties of MoO3: An in situ Raman Spectroscopy Study. *Journal of physical chemistry (1952)* **1994**, *98* (44), 11269-11275. DOI: 10.1021/j100095a007.
- (45) Mestl, G.; Verbruggen, N.; Bosch, E.; Knözinger, H. Mechanically activated MoO3. 5. Redox behavior. *Langmuir* **1996**, *12* (12), 2961-2968.
- (46) Dieterle, M.; Weinberg, G.; Mestl, G. Raman spectroscopy of molybdenum oxides Part I. Structural characterization of oxygen defects in MoO 3– x by DR UV/VIS, Raman spectroscopy and X-ray diffraction. *Physical Chemistry Chemical Physics* **2002**, *4* (5), 812-821.
- (47) Matthews, M. J.; Pimenta, M. A.; Dresselhaus, G.; Dresselhaus, M.; Endo, M. Origin of dispersive effects of the Raman D band in carbon materials. *Physical review B* **1999**, *59* (10), R6585.
- (48) Dong, Y.; Xu, X.; Li, S.; Han, C.; Zhao, K.; Zhang, L.; Niu, C.; Huang, Z.; Mai, L. Inhibiting effect of Na+ pre-intercalation in MoO3 nanobelts with enhanced electrochemical performance. *Nano energy* **2015**, *15*, 145-152. DOI: 10.1016/j.nanoen.2015.04.015.
- (49) Dunkin, M. R.; Kuang, J.; Yan, S.; King, S. T.; Housel, L. M.; Ma, L.; Ehrlich, S. N.; Okasinski, J. S.; Takeuchi, K. J.; Takeuchi, E. S.; et al. Unveiling Charge Transport and Degradation Mechanisms of Aqueous Zn|α-MoO3 Batteries in Conventional Concentration and Water-in-Salt Electrolytes: A Multi-Modal In Situ and Operando Study. *Advanced Materials Interfaces* **2022**, *9* (29), 2201125. DOI: 10.1002/admi.202201125.